Exceptional-point restoration and fast-light edge states in photonic crystal waveguides with glide and time-reversal symmetries

Takahiro Uemura,[1,2] Taiki Yoda,[1] Yuto Moritake,[1] Shutaro Otsuka,[1,2] Kenta Takata,[2,3] and Masaya Notomi[1,2,3,*]

[1]*Department of Physics, Tokyo Institute of Technology, 2-12-1 Ookayama, Meguro-ku, Tokyo 152-8551, Japan*

[2]*NTT Basic Research Laboratories, NTT Corporation, 3-1 Morinosato-Wakamiya, Atsugi-shi, Kanagawa 243-0198, Japan*

[3]*Nanophotonics Center, NTT Corporation, 3-1, Morinosato-Wakamiya, Atsugi-shi, Kanagawa 243-0198, Japan*

(Received 24 October 2024; accepted 27 February 2025; published 14 March 2025)

Exceptional points (EPs) in propagation states induce intriguing properties as the group velocities. However, superluminal propagation near EPs is challenging due to the smoothing caused by symmetry breaking. In this study, we propose a photonic crystal waveguide design with glide and time-reversal symmetry and derive an effective Hamiltonian to realize fast-light edge states. We adopt a systematic method to generate EPs in edge states by introducing non-Hermitian perturbations to Dirac points guaranteed by glide symmetry, which ensures that EP modes are free from out-of-plane radiation losses. We identify the conditions for exact EP restoration and provide an analytical solution to offset the EP smoothing due to symmetry breaking, which significantly reduces the group velocity contrast. A glide symmetry of the photonic crystal waveguide allows us to derive the effective Hamiltonian in a simple form, and the EPs can be restored by adjusting the real part of the permittivity. Furthermore, we design a feasible photonic crystal slab waveguide incorporating graphene as the absorbing material, and numerically demonstrate a group velocity reaching $v_g = 3.3c$ near the EP, which is up to 25 times that of the original structure. The proposed setup based on non-Hermitian photonics paves the way for the realization of superluminal devices in nanophotonics. In addition, the method for restoring EPs also addresses challenges in the phenomena arising from non-Hermitian properties.

DOI: 10.1103/PhysRevA.111.033513

I. INTRODUCTION

Non-Hermitian optical systems have gained interest as a new approach for controlling light, and $\mathcal{PT}$-symmetric systems, which exhibit symmetry in spatial parity and time inversion, have received considerable attention [1,2]. $\mathcal{PT}$-symmetric optical systems are significant for implementing complex potentials using optical gain from lasers [3] or current injection [4], coupled with radiation or material absorption loss [5–7]. $\mathcal{PT}$-symmetric systems have been used to realize various optical phenomena, including nonreciprocal transmission [8], enhanced sensing [9], single-mode lasing [10,11], and loss-induced transparency [12].

In the context of periodic potential structures, it has been noted that the slope of the band diverges in the vicinity of the exceptional point (EP) [13]. Controlling light propagation is a fundamental aspect of photonics, and manipulation of the group velocity is a central technology for the advancement of optical devices. Recent advancements in semiconductor microfabrication technology have enabled the realization of on-chip slow light in nanophotonics [14], including resonator-type coupled resonator optical waveguides (CROWs) [15–17] and photonic crystal waveguides [18–20]. Conversely, light propagating with a group velocity faster than the speed of light in vacuum, known as fast light, has been observed in media with anomalous dispersion near an absorption line [21] and atomic systems [22,23], as well as in artificial media such as metamaterials [24,25]. However, achieving fast light in conventional transparent media for on-chip waveguides remains challenging. The concept of $\mathcal{PT}$-symmetric optical waveguide systems exhibits the potential to introduce a breakthrough in achieving fast light in on-chip waveguides.

While such interesting properties in $\mathcal{PT}$-symmetric optical waveguide system have been predicted, the realization of fast light in $\mathcal{PT}$-symmetric systems remain challenging. The anomalous group velocity near EPs, referred to as fast light, has been discussed in Refs. [26,27]. Reference [28] theoretically investigated fast light in $\mathcal{PT}$-symmetric systems and implemented it numerically in CROW structures using photonic crystal cavity arrays. However, the low group velocity and strong light confinement make it difficult to apply CROW to fast-light propagation states. The initial group velocities of the modes in CROW are inherently slow ($v_g = 0.02c$ with periods of 2.1 μm [28]). Specifically, group velocities exceeding the speed of light in vacuum have an order of $100v_g$, which requires extremely precise control of spatial structures, gains, and losses. Moreover, the strong light confinement in the cavity makes it increasingly difficult to achieve high fabrication precision. The issues related to group velocity and fabrication precision can be resolved by weakening the light confinement to increase the coupling rate between the resonators, even if the period of the cavity is large. However, this approach is contrary to the typical CROW configuration. CROW with wide periods and weak light confinement can be regarded as photonic crystals with large periods. Very high-order bands

*Contact author: notomi@phys.titech.ac.jp

are thus used as as a photonic crystals, which is not advantageous compared to using conventional $\mathcal{PT}$-symmetric photonic crystal waveguides. In addition, it should be noted that the waveguide modes of CROW are positioned above the light line, and their influence depends on the Q factor. Specifically, it is inherently difficult to eliminate the effects of out-of-plane radiation losses from the waveguide modes of CROW.

Therefore, our research motivation lies in realizing superluminal states with a group velocity contrast of one digit from the initial edge states leveraging the $\mathcal{PT}$ symmetry in photonic crystal waveguide systems, which have significantly shorter periods on the order of submicrometers. Photonic crystal waveguides offer additional advantages over CROW in terms of scalability and device integration, making them favorable for applications in optical devices. However, adopting photonic crystal band systems presents challenges not encountered in CROW, where the EP smoothing due to finite Q can be canceled using a tight-binding-based formalism [29]. In contrast to tight-binding systems, the restoration mechanism for EPs smoothed by symmetry breaking is not known. Therefore, establishing an EP restoration method in photonic crystal systems is a significant step towards the realization of superluminal propagation states. Since the use of photonic crystal bulk modes as waveguide modes is not realistic, the focus of our study is on edge states in photonic crystal waveguides. Several methods for realizing photonic crystal waveguides have been proposed, such as using a degenerate point created by imaginary perturbations and unit cell enlargement [30,31], an accidental degenerate point [31,32], and symmetry-protected degenerate points [31]. The first and second methods make it challenging to position the EP below the light line. In contrast, the third method allows the EP to be positioned below the light line, which ensures that the propagation modes near the EP are free from out-of-plane radiation loss. Additionally, the third method allows for an analytical solution of the effective Hamiltonian owing to its suitable symmetry properties, making it easier to develop methods to restore the EP when the symmetry is broken. This phenomenon has not been noted in Ref. [31].

In this paper, we propose a photonic crystal waveguide with symmetry under simultaneous glide and time-reversal operations. Our scheme starts with the generation of EPs using a systematic approach with $\mathcal{PT}$-symmetric perturbations at Dirac points, which appear due to the spatial glide symmetry [33–35]. The EPs appear at the boundary of the Brillouin zone, providing two key advantages, both of which address issues inherent to traditional $\mathcal{PT}$-symmetric photonic crystal waveguides [30–32]. The first advantage is that the EPs can be positioned below the light line, ensuring that the propagation modes near the EP are free from out-of-plane radiation loss. This is in contrast to most structures proposed in previous studies, such as [31], where EP smoothing could not be avoided due to radiation loss, which significantly reduced the group velocity contrast. The second advantage is that the symmetry at the boundary of the Brillouin zone allows the $\boldsymbol{k}\cdot\boldsymbol{p}$ Hamiltonian around the EPs to be represented in a simplified form, making it easier to model the response of edge states to non-Hermitian perturbations. EPs in our waveguide are sensitive to glide deformations and time-reversal symmetry, which makes it challenging to achieve high group velocity contrast. Therefore, we derive the precise EP conditions for complex permittivity perturbations, which are essential for realizing superluminal propagation states. In addition to the above advantages, we adopt the valley photonic crystal waveguide as the basic structure, which exhibits suitable topological properties and has the potential for future applications in optical circuits with bends [36]. Moreover, the proposed structure is characterized by its ease of fabrication. Our design can be implemented by selectively loading graphene along the glide plane of a photonic crystal slab waveguide, which is simpler than embedded heterostructures that require precise gain and loss adjustments. Our study contributes to experimental observations of superluminal propagation states in on-chip non-Hermitian nano-optical systems. Furthermore, our proposed method for suppressing EP smoothing has the potential to contribute to the exploitation of the EPs beyond superluminal phenomena, including sensing [9] and nonreciprocal devices [8].

II. DESIGN OF NON-HERMITIAN PHOTONIC CRYSTAL WAVEGUIDES WITH GLIDE AND TIME-REVERSAL SYMMETRY

First, we present the design of our photonic crystal heterostructure based on two-dimensional (2D) simulation, where the system extends infinitely along the z axis. All numerical calculations in this paper were performed using the finite element method (FEM) in COMSOL Multiphysics.

We start from the design of a glide symmetric photonic crystal heterostructure with triangular lattice and triangular holes, as shown in Fig. 1(a). This is also known as the bearded edge of the photonic crystal [37]. We also considered other types of lattices and hole shapes (Appendix A), but adopted the triangular lattice and triangular holes because we found that the Dirac points can be easily located inside the band gap and below the light line. The difference between triangular and circular holes lies in the presence or absence of valley-polarized features near the K(K′) point in the bulk band, and there is no essential difference for contraction of EPs in edge states. We set the lattice constant as $a = 470$ and triangular hole side as $s = 0.8a$. The air and slab permittivity are set to $\varepsilon_{\text{air}} = 1$ and $\varepsilon_{\text{slab}} = 6.76$, respectively. The value of $\varepsilon_{\text{slab}}$ corresponds to an effective refractive index of typical semiconductor materials such as silicon and compound semiconductor materials. The dashed line in Fig. 1(a) represents the glide symmetric plane, and we define it as $y = 0$ and establish our coordinate axis accordingly. The heterostructure is invariant under a glide operation with the xz plane, which is a combination of a reflection with the xz plane and translation along the x axis. The glide operator is given by

$$\hat{G} = \left\{m_y \middle| \tfrac{1}{2}\hat{\mathrm{x}}\right\}, \tag{1}$$

where m_y and $\hat{\mathrm{x}}$ represent mirror reflection with respect to the xz plane and a unit vector along the x axis, respectively. Let $\varepsilon(\boldsymbol{r})$, $\boldsymbol{r} = [x, y, z]^\top$ be the permittivity of initial photonic crystal, and $\varepsilon(\boldsymbol{r})$ is invariant with respect to the glide operation:

$$\hat{G}\varepsilon(\boldsymbol{r}) = \varepsilon\left(x + \frac{a}{2}, -y, z\right) = \varepsilon(\boldsymbol{r}). \tag{2}$$

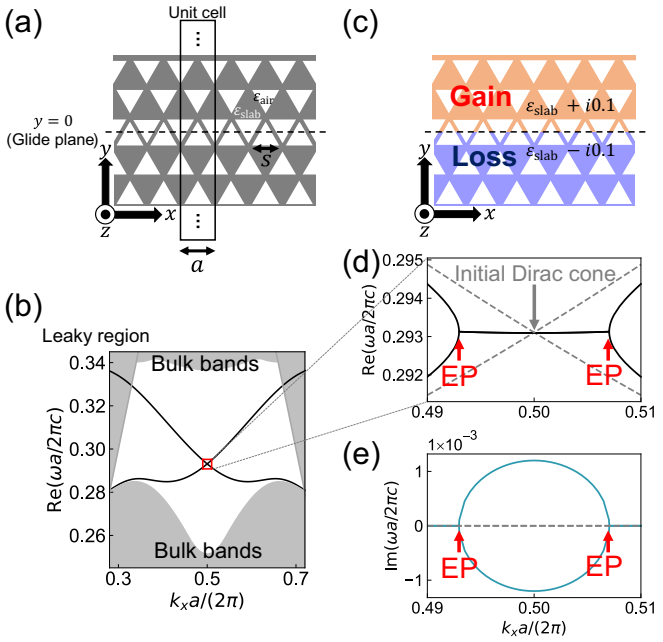

FIG. 1. (a) Interface geometry of the photonic crystal heterostructure with the triangular lattice and triangular holes. This structure has glide symmetry along the $y = 0$ plane, as shown by the dashed line. (b) The band dispersion curves in the k_x direction of the TE mode in geometry (a). (c) Interface geometry of the glide symmetric photonic crystal heterostructure with balanced gain ($y > 0$) and loss ($y < 0$). This structure is invariant under both a glide operation with the xz plane and a simultaneous time-reversal operation. (d), (e) The real and imaginary parts of band dispersion curves along the k_x direction near $k_x a = \pi$.

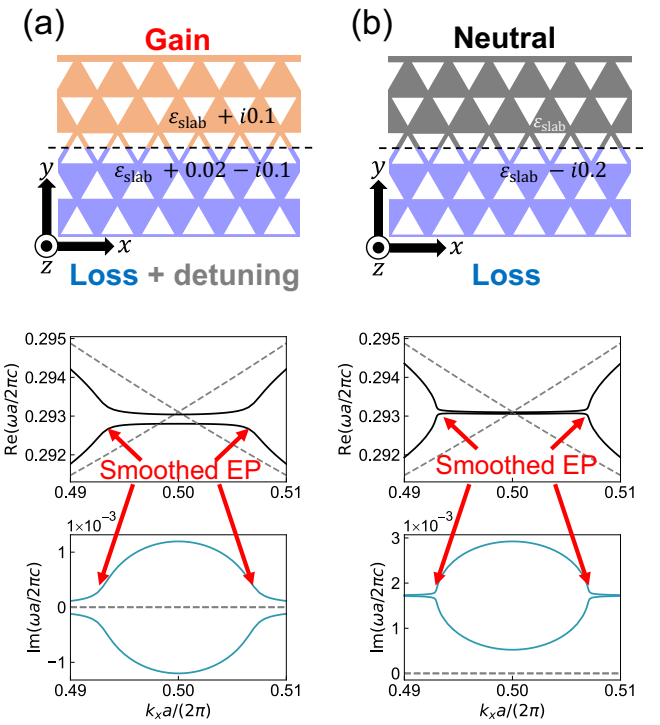

FIG. 2. (a) Interface geometry and corresponding band dispersion curves along the k_x direction of the photonic crystal heterostructure with symmetric gain ($y > 0$) and loss ($y < 0$), but asymmetrical detuning of real part of permittivity. (b) Interface geometry and corresponding band dispersion curves with loss ($y < 0$).

The band dispersion curves of the TE mode along the k_x axis are shown in Fig. 1(b). The region shaded in gray represents the area outside the bulk band and beyond the light line. The existence of the Dirac point at $k_x a = \pi$ in the band dispersion is guaranteed by the spatial glide symmetry of the photonic crystal [19,38,39].

The key point of our design is to introduce a gain on the upper side and a loss of the same magnitude on the lower side, bordering the glide plane. Figure 1(c) shows the interface geometry of the photonic crystal heterostructure with balanced gain ($y > 0$) and loss ($y < 0$). The perturbation of the imaginary part of the permittivity are set to $\Delta\varepsilon_i(\boldsymbol{r}) = 0.1 \times 1_{\boldsymbol{r}\in \text{slab} \cap y>0}$ (gain) and $\Delta\varepsilon_i(\boldsymbol{r}) = 0.1 \times 1_{\boldsymbol{r}\in \text{slab} \cap y<0}$ (loss). Let $\hat{T}$ be the time-reversal operator; then the perturbed permittivity $\varepsilon'(\boldsymbol{r}) = \varepsilon(\boldsymbol{r}) + \Delta\varepsilon(\boldsymbol{r})$ has a symmetry with respect to the simultaneous operation of $\hat{G}$ and $\hat{T}$:

$$(\hat{G}\hat{T})\varepsilon'(\boldsymbol{r}) = (\hat{T}\hat{G})\varepsilon'(\boldsymbol{r}) = \varepsilon'(\boldsymbol{r}). \tag{3}$$

Figures 1(d) and 1(e) show the real and imaginary parts of the band dispersion near $k_x a = \pi$, respectively. The Dirac point splits into two EPs when the gain and loss are balanced owing to the glide and time-reversal (GT) symmetries. Note that the glide operation on our system corresponds to the parity inversion operation in the context of $\mathcal{PT}$-symmetric optical systems. The edge states undergo a phase transition between the $\mathcal{PT}$-symmetric and $\mathcal{PT}$-broken phases, as in general $\mathcal{PT}$-symmetric optical systems. Appendix B provides the details with the H_z distribution of the edge state. Our approach is advantageous because it allows for the systematic generation of EPs in the band dispersion of waveguide edge states. In addition, the initial Dirac point is located in the band gap, which favors waveguide applications.

III. RECONSTRUCTION OF EXACT EPS BASED ON PERTURBATION THEORY

In the previous sections we discussed the situation with glide and time-reversal symmetries. It should be noted that the EP is sensitive to symmetry breaking; any detuning that breaks the glide and time-reversal symmetries lifts the EP and smoothens the band dispersion near the EP. For example, as shown in Fig. 2(a), when a detuning of the real part of the permittivity, $\text{Re}(\Delta\varepsilon) = 0.02$, is applied to the region of the dielectric where $y < 0$, the EP lifts and the band dispersion curves near the initial EP are smoothed. In addition, as shown in Fig. 2(b), introducing only loss in the dielectric region where $y < 0$ also breaks the glide and time-reversal symmetries due to the imbalance of gain and loss. "Passive" systems with only loss are advantageous for simple fabrication processes [40], but it is known that EPs are smoothed due to the the imaginary coupling of each eigenstate [29]. In any case, EP smoothing significantly reduces the group velocity contrast, which is a critical issue for realizing superluminal propagation states. Therefore, it is essential to develop methods to restore the EP by counteracting the effects of symmetry breaking. While Ref. [29] provides theoretical analysis and

methods to offset the EP smoothing in CROW systems, photonic crystal waveguide systems have not been investigated in this context to the best of our knowledge.

Here we derive an effective Hamiltonian using the $\boldsymbol{k}\cdot\boldsymbol{p}$ perturbation method to model the bands of the edge states near the original Dirac point, that is, $k_x a = \pi$. Furthermore, based on the $\boldsymbol{k}\cdot\boldsymbol{p}$ Hamiltonian, we derive the precise EP conditions for complex permittivity perturbations, and show that EPs can always be restored even in passive photonic crystal waveguides by adjusting of the real part of the permittivity.

A. Effective Hamiltonian of edge states near the Dirac point

This section describes the derivation of the effective Hamiltonian that models the band dispersion of edge states in the photonic crystal waveguide near the Dirac point. We consider two types of perturbations: one is the detuning of the wave vector from the Dirac point $\boldsymbol{\delta k} = [k_x - k_0, 0, 0]^\top$, and the other denotes the permittivity perturbation $\Delta\varepsilon(\boldsymbol{r})$. For simplicity, we consider that the permittivity perturbation is pure imaginary $\Delta\varepsilon(\boldsymbol{r}) \in i\mathbf{R}$. We define the two unperturbed bases $\boldsymbol{\varphi}^{(0)}_{\alpha k_0}(\boldsymbol{r})$ and $\boldsymbol{\psi}^{(0)}_{\alpha k_0}(\boldsymbol{r})$ as the normalized electric and magnetic fields at $k_x = \pi/a$ with $\Delta\varepsilon(\boldsymbol{r}) = 0$. Here α denotes the label of the basis, and C_α denotes the expansion coefficients of the basis. The two bases are degenerated at the Dirac point due to the glide symmetry of the unperturbed photonic crystal.

The $\boldsymbol{k}\cdot\boldsymbol{p}$ Hamiltonian for the edge states near the Dirac point is given by the following 2×2 matrix form (Appendix C):

$$\begin{bmatrix} \left(\frac{\omega^{(0)}_\alpha}{c}\right)^2 + P'_{\alpha\alpha} + Q'_{\alpha\alpha} & P'_{\alpha\beta} + Q'_{\alpha\beta} \\ P'_{\beta\alpha} + Q'_{\beta\alpha} & \left(\frac{\omega^{(0)}_\beta}{c}\right)^2 + P'_{\beta\beta} + Q'_{\beta\beta} \end{bmatrix} \begin{bmatrix} C_\alpha \\ C_\beta \end{bmatrix} = \left(\frac{\omega_{nk}}{c}\right)^2 \begin{bmatrix} 1+G_{\alpha\alpha} & G_{\alpha\beta} \\ G_{\beta\alpha} & 1+G_{\beta\beta} \end{bmatrix} \begin{bmatrix} C_\alpha \\ C_\beta \end{bmatrix}. \tag{4}$$

Here c is the speed of light in vacuum, ω_{nk} represents the eigenfrequency of the nth mode, α and β denote the label of the eigenmodes, $\omega^{(0)}_\alpha$, $\omega^{(0)}_\beta$ denote the unperturbed frequencies, and $\omega^{(0)}_\alpha = \omega^{(0)}_\beta$ holds regardless of the choice of the bases due to the degeneracy by the glide symmetry. $P'_{\alpha\beta}$, $G_{\alpha\beta}$, and $Q'_{\alpha\beta}$ are defined as follows:

$$P'_{\alpha\beta} = \int_{\text{u.c.}} \left[\omega^{(0)}_\beta \boldsymbol{\psi}^{(0)*}_{\alpha k_0}(\boldsymbol{r}) \times \boldsymbol{\varphi}^{(0)}_{\beta k_0}(\boldsymbol{r}) - \omega^{(0)}_\alpha \boldsymbol{\varphi}^{(0)*}_{\alpha k_0}(\boldsymbol{r}) \times \boldsymbol{\psi}^{(0)}_{\beta k_0}(\boldsymbol{r})\right] \cdot \boldsymbol{\delta k}\, \mathrm{d}^3 r, \tag{5}$$

$$G_{\alpha\beta} := \int_{\text{u.c.}} \mathrm{d}^3 r \Delta\varepsilon(\boldsymbol{r}) \boldsymbol{\psi}^{(0)*}_{\alpha k_0}(\boldsymbol{r}) \cdot \boldsymbol{\psi}^{(0)}_{\beta k_0}(\boldsymbol{r}), \tag{6}$$

$$Q'_{\alpha\beta} = -\int_{\text{u.c.}} \boldsymbol{\psi}^{(0)*}_{\alpha k_0}(\boldsymbol{r}) \cdot \left[\boldsymbol{\delta k} \times \boldsymbol{\delta k} \times \boldsymbol{\psi}^{(0)}_{\beta k_0}(\boldsymbol{r})\right] \mathrm{d}^3 r. \tag{7}$$

The $\boldsymbol{k}\cdot\boldsymbol{p}$ perturbation generally describes the response of frequencies and eigenstates to the perturbation of the wave vector $\boldsymbol{\delta k}$. However, the response of the band to the perturbation $\Delta\varepsilon(\boldsymbol{r})$ is also naturally incorporated in $G_{\alpha\beta}$. Considering that $\boldsymbol{\delta k}$ only has a k_x component, $P'_{\alpha\beta}$ and $Q'_{\alpha\beta}$ can be expressed using scalars $P_{\alpha\beta}$ and $Q_{\alpha\beta}$, which are independent of the wave number δk_x, as follows:

$$P'_{\alpha\beta} = P_{\alpha\beta}\delta k_x, \quad Q'_{\alpha\beta} = Q_{\alpha\beta}(\delta k_x)^2. \tag{8}$$

$P_{\alpha\beta}$ and $Q_{\alpha\beta}$ are given by

$$P_{\alpha\beta} = \int_{\text{u.c.}} \left[\omega^{(0)}_\beta \boldsymbol{\psi}^{(0)*}_{\alpha k_0}(\boldsymbol{r}) \times \boldsymbol{\varphi}^{(0)}_{\beta k_0}(\boldsymbol{r}) - \omega^{(0)}_\alpha \boldsymbol{\varphi}^{(0)*}_{\alpha k_0}(\boldsymbol{r}) \times \boldsymbol{\psi}^{(0)}_{\beta k_0}(\boldsymbol{r})\right]_x \mathrm{d}^3 r, \tag{9}$$

$$Q_{\alpha\beta} = \int_{\text{u.c.}} \left\{\left[\psi^{(0)*}_{\alpha k_0}(\boldsymbol{r})\right]_y \left[\psi^{(0)}_{\beta k_0}(\boldsymbol{r})\right]_y + \left[\psi^{(0)*}_{\alpha k_0}(\boldsymbol{r})\right]_z \left[\psi^{(0)}_{\beta k_0}(\boldsymbol{r})\right]_z\right\} \mathrm{d}^3 r. \tag{10}$$

While $G_{\alpha\beta}$ represents the effect of permittivity perturbation on the bands, $P_{\alpha\beta}$ and $Q_{\alpha\beta}$ are determined exclusively by the unperturbed photonic crystal.

Next, we simplify Eq. (4) using the mirror symmetry along the x axis, which is independent of the glide symmetry. We set the unit cell as shown in Fig. 2(a), and the x axis as the center of the unit cell. Since the initial permittivity and perturbation are symmetric about the x axis, $\varepsilon(\boldsymbol{r})$ and $\Delta\varepsilon(\boldsymbol{r})$ in the unit cell are invariant under the mirror operation with respect to the yz plane:

$$\hat{M}_x[\varepsilon(\boldsymbol{r})] = \varepsilon(-x, y, z) = \varepsilon(x, y, z), \tag{11}$$

$$\hat{M}_x[\Delta\varepsilon(\boldsymbol{r})] = \Delta\varepsilon(-x, y, z) = \Delta\varepsilon(x, y, z). \tag{12}$$

Here $\hat{M}_x$ is the mirror operator with respect to the yz plane. Note that the assumption that the initial permittivity is symmetric about the x axis [Eq. (12)] is generally satisfied in typical photonic crystal lattices such as triangular, square, and honeycomb lattices. Then the two eigenmodes can be classified into the following two categories according to the eigenvalues for operator $\hat{M}_x$:

$$\hat{M}_x\left[\boldsymbol{\varphi}^{(0)}_{ik_0}(x, y, z)\right]_z = \left[\boldsymbol{\varphi}^{(0)}_{ik_0}(-x, y, z)\right]_z = \pm\left[\boldsymbol{\varphi}^{(0)}_{ik_0}(x, y, z)\right]_z, \quad i \in \{\text{u}, \text{d}\}. \tag{13}$$

There is an arbitrary choice of the basis functions of the eigenmodes at $k_x = \pi/a$ since the band dispersion curves are degenerate at the Dirac point, and we select the basis functions $\boldsymbol{\varphi}^{(0)}_{\text{u}k_0}(\boldsymbol{r})$, $\boldsymbol{\varphi}^{(0)}_{\text{d}k_0}(\boldsymbol{r})$, which are characterized by the mirror eigenvalues -1 and 1:

$$\hat{M}_x\left[\boldsymbol{\varphi}^{(0)}_{\text{u}k_0}(\boldsymbol{r})\right]_z = -\left[\boldsymbol{\varphi}^{(0)}_{\text{u}k_0}(\boldsymbol{r})\right]_z, \tag{14}$$

$$\hat{M}_x\left[\boldsymbol{\varphi}^{(0)}_{\text{d}k_0}(\boldsymbol{r})\right]_z = \left[\boldsymbol{\varphi}^{(0)}_{\text{d}k_0}(\boldsymbol{r})\right]_z. \tag{15}$$

From the relationship of the electric and magnetic fields of the eigenmodes, the symmetry of H_z, E_x, E_y at the Dirac point is summarized in Table I. According to the even or odd symmetry of the electromagnetic field components, as shown in Table I,

$$P_{\text{uu}} = P_{\text{dd}} = G_{\text{ud}} = G_{\text{du}} = Q_{\text{ud}} = Q_{\text{du}} = 0 \tag{16}$$

holds when conditions (11) and (12) are satisfied. Moreover, we get $(P_{\text{ud}})_x = -(P_{\text{du}})_x =: -iP$, $P \in \mathbf{R}$ from the time-reversal symmetry of the initial structure, and

TABLE I. The symmetry along the y axis of the eigenmodes at the Dirac point. The value of 1 or -1 represents the symmetric and antisymmetric, respectively.

	u	d
H_z	-1	1
E_x	-1	1
E_y	1	-1

$Q_{\mathrm{uu}} = Q_{\mathrm{dd}} =: Q$ from the mirror symmetry. Therefore, Eq. (4) is reduced to the following form:

$$\begin{bmatrix} F & iP\delta k_x \\ -iP\delta k_x & F \end{bmatrix}\begin{bmatrix} C_{\mathrm{u}} \\ C_{\mathrm{d}} \end{bmatrix} = \left(\frac{\omega_{nk}}{c}\right)^2 \begin{bmatrix} 1+G_{\mathrm{uu}} & 0 \\ 0 & 1+G_{\mathrm{dd}} \end{bmatrix}\begin{bmatrix} C_{\mathrm{u}} \\ C_{\mathrm{d}} \end{bmatrix}, \tag{17}$$

$$F := \left(\frac{\omega_D}{c}\right)^2 + Q(\delta k_x)^2. \tag{18}$$

Here ω_D is the eigenfrequency of two eigenmodes at the Dirac point, and P corresponds to the slope of the band dispersion curves at $k_x a = \pi$. Furthermore, multiply the inverse of the diagonal matrix from the left to eliminate the matrix from the right side of the equation, and let

$$\begin{aligned} \Delta G &:= \frac{G_{\mathrm{dd}} - G_{\mathrm{uu}}}{2} \\ &= \frac{1}{2}\int_{\mathrm{u.c.}} \mathrm{d}^3 r \Delta\varepsilon(\boldsymbol{r})\left(\left|\boldsymbol{\psi}^{(0)}_{\mathrm{d}k_0}(\boldsymbol{r})\right|^2 - \left|\boldsymbol{\psi}^{(0)}_{\mathrm{u}k_0}(\boldsymbol{r})\right|^2\right), \end{aligned} \tag{19}$$

then we get the following form:

$$\begin{aligned} &\left[F\left(1+\frac{G_{\mathrm{uu}}+G_{\mathrm{dd}}}{2}\right)I_2 + H'\right]\begin{bmatrix} C_{\mathrm{u}} \\ C_{\mathrm{d}} \end{bmatrix} = E_{nk}\begin{bmatrix} C_{\mathrm{u}} \\ C_{\mathrm{d}} \end{bmatrix}, \\ &H' = \begin{bmatrix} F\Delta G & i(1+G_{\mathrm{dd}})P\delta k_x \\ -i(1+G_{\mathrm{uu}})P\delta k_x & -F\Delta G \end{bmatrix}. \end{aligned} \tag{20}$$

Here I_2 is a 2×2 identity matrix, and $E_{nk} := (1+G_{\mathrm{uu}})(1+G_{\mathrm{dd}})(\omega_{nk}/c)^2$ denotes the eigenvalues. H' in Eq. (20) characterizes the band structure of the edge states. The diagonal term $\pm(\omega_D/c)^2\Delta G$ in Eq. (20) is regarded as the difference between the potentials of $y > 0$ and $y < 0$. More specifically, ΔG is proportional to the difference between two norms of the basis functions in the perturbed region. Furthermore, the off-diagonal terms $i(1+G_{\mathrm{dd}})P$, $-i(1+G_{\mathrm{uu}})P$ in H' represent the complex couplings of two basis. Note that it is fundamentally important for the simplicity of the Hamiltonian due to Eq. (16) that the basis u and d are degenerated due to the glide symmetry, and that they also possess (anti-)symmetry with respect to $\hat{M}_x$.

The corresponding eigenvalues E_{nk} are given by the following equation:

$$\begin{aligned} E_{nk} &= F\left(1+\frac{G_{\mathrm{uu}}+G_{\mathrm{dd}}}{2}\right) \\ &\pm\sqrt{(F\Delta G)^2 + (1+G_{\mathrm{uu}})(1+G_{\mathrm{dd}})(P\,\delta k_x)^2}. \end{aligned} \tag{21}$$

The sign of the square root in Eq. (21) corresponds to the solution number of the eigenvalues $n = 1, 2$. From the form of eigenvalues in Eq. (21), the corresponding EP condition is given by

$$\frac{P(\delta k_x)^2}{\left[\left(\frac{\omega_D}{c}\right)^2 + Q(\delta k_x)^2\right]^2} = \frac{-(\Delta G)^2}{(1+G_{\mathrm{uu}})(1+G_{\mathrm{dd}})}. \tag{22}$$

All of the components in the left-hand side of Eq. (22) are real numbers; there exist EPs in the real δk_x space when the right-hand side of Eq. (22) is positive. The right-hand side of Eq. (22) is always positive as long as the system has the glide and time-reversal symmetry, since ΔG is pure imaginary and the $(1+G_{\mathrm{uu}})(1+G_{\mathrm{dd}})$ is a real number because $G^*_{\mathrm{uu}} = G_{\mathrm{dd}}$ holds. Equation (22) indicates that the EPs under the glide and time-reversal symmetry always exist near $k_x = \pi/a$, which means that EP is always located below the light line.

Although the initial form of Hamiltonian shown in Eq. (4) has the similar form in Ref. [41], the derived Hamiltonian shown in Eq. (20) and the physical interpretation are entirely different. Their model targets the bulk bands in the photonic crystals and utilizes the band folding with double-period imaginary perturbations. The band folding places the EP above the light line, which makes it difficult to use as a waveguide mode. In contrast, our system is a photonic crystal waveguide with edge states, which allows the EP to utilize the waveguide mode. Furthermore, the design with glide symmetry allows the EP to be located below the light line, which ensures that the EP modes are free from out-of-plane radiation loss. This aspect highlights an advantage of our scheme compared to the waveguide structures proposed in Refs. [30–32]. The configuration for numerical analysis and the comparison between FEM and $\boldsymbol{k}\cdot\boldsymbol{p}$ approximation are as follows. Figures 3(a) and 3(b) show the computational setup and the magnetic field of the two bases, respectively. We can see that $|\boldsymbol{\varphi}_{\mathrm{u}}(\boldsymbol{r})|^2$ and $|\boldsymbol{\varphi}_{\mathrm{d}}(\boldsymbol{r})|^2$, which are proportional to $|\boldsymbol{H}|^2$, are localized at the upper and lower sites, respectively. Figure 3(c) shows the H_z, E_x, and E_y distribution of the bases at the Dirac point defined by Eqs. (14) and (15). It is clear the H_z and E_x distribution of mode u are antisymmetric along the y axis, while the E_y distribution is symmetric along the y axis. Moreover, the opposite is true for mode d. These results are consistent with the classification of the eigenmodes based on the mirror symmetry along the x axis in Table I. The band dispersion in a heterostructure with the $\mathcal{PT}$-symmetric permittivity perturbation using the FEM method and $\boldsymbol{k}\cdot\boldsymbol{p}$ Hamiltonian is shown in Fig. 4(a). The black circle and blue triangle points represent the real and imaginary parts of the eigenvalues obtained by FEM, and the black and blue lines represent the real and imaginary parts by the $\boldsymbol{k}\cdot\boldsymbol{p}$ Hamiltonian. No fitting is used to obtain the coefficients in the $\boldsymbol{k}\cdot\boldsymbol{p}$ Hamiltonian; instead, the coefficients are determined using two unperturbed bases $\boldsymbol{\varphi}^{(0)}_{\alpha k_0}(\boldsymbol{r})$ and $\boldsymbol{\psi}^{(0)}_{\alpha k_0}(\boldsymbol{r})$ calculated by FEM and Eqs. (6), (9), and (10). The band dispersion show the good agreement between the $\boldsymbol{k}\cdot\boldsymbol{p}$ and FEM methods. Moreover, the EPs are clearly observed in the real δk_x space, which is consistent with the theoretical prediction.

B. Restoration of EP by adjusting the real part of the permittivity

Next, we describe how to restore the EP in the case where the EP is smoothed out by breaking the glide and time-reversal

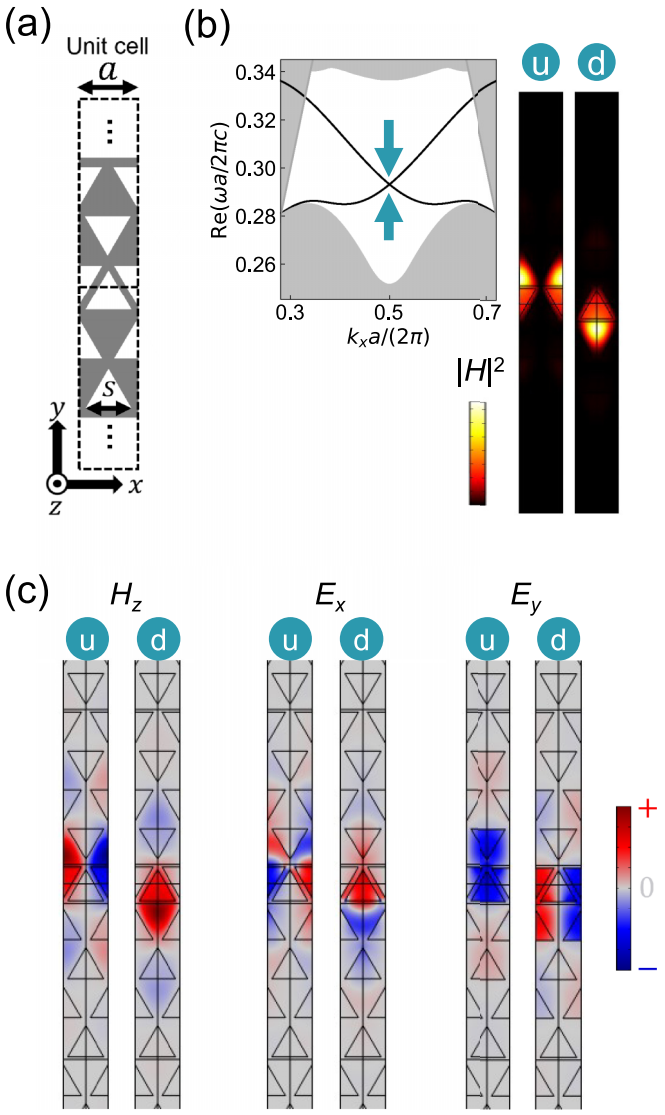

FIG. 3. (a) The configuration of the photonic crystal heterostructure to obtain the eigenmodes at the Dirac point used for the $\boldsymbol{k}\cdot\boldsymbol{p}$ Hamiltonian. (b) $|\boldsymbol{H}|^2$ distribution of the eigenmodes in the photonic crystal heterostructure. Labels u and d denote $\boldsymbol{\varphi}^{(0)}_{uk_0}$, $\boldsymbol{\varphi}^{(0)}_{dk_0}$, respectively. (c) H_z, E_x, and E_y distribution of the bases at the Dirac point.

symmetry. It is obvious that if there is a mismatch in the real part of the permittivity on both sides of the glide plane, as shown in Fig. 2(a), the EP can be restored by simply adjusting the real part of the permittivity that compensates for the difference. Mathematically, this can be explained as follows: when there is a mismatch in the real part of the permittivity, ΔG defined in Eq. (19) becomes a complex number, and the EP condition shown in Eq. (22) is no longer satisfied. By compensating for the real part of the permittivity, ΔG becomes a pure imaginary number again, and the EP is restored. In contrast to the situation, the way to restore the EP in the presence of gain-loss imbalance is not trivial. The gain-loss imbalance breaks the EP condition since $G^*_{uu} \neq G_{dd}$ holds and $(1+G_{uu})(1+G_{dd})$ becomes a complex number. The situation has the same mathematical origin as the EP smoothing due to the complex coupling between the two basis in a coupled resonator array [29].

The following discussion will focus on the case where the uniform imaginary part of the permittivity $\Delta\varepsilon_i$ is introduced for the dielectric region where $y<0$ [V_G as shown in the blue region in Figs. 1(b) and 1(c)], which is responsible for the non-Hermitian perturbation. Moreover, the real part of the permittivity perturbation $\Delta\varepsilon_r$ is introduced for V_G to restore the EP.

Let $I_{\alpha\beta}$, $J_{\alpha\beta}$, and κ be defined as follows:

$$I_{\alpha\beta} := \int_{\boldsymbol{r}\in V_G} \boldsymbol{\psi}^{(0)*}_{\alpha k_0}(\boldsymbol{r})\cdot\boldsymbol{\psi}^{(0)}_{\beta k_0}(\boldsymbol{r})\,\mathrm{d}^3 r,$$
$$J_{\alpha\beta} := \Delta\varepsilon_{\mathrm{i}} I_{\alpha\beta}, \quad \kappa := \frac{\Delta\varepsilon_{\mathrm{r}}}{\Delta\varepsilon_{\mathrm{i}}}. \tag{23}$$

From the following definition, we get $G_{\alpha\beta} = (\kappa + i)J_{\alpha\beta}$. The necessary condition for $-(\Delta G)^2/(1+G_{uu})(1+G_{dd})$ to be a positive real number, which is the condition for the existence of EP shown in Eq. (22), is that the vectors of the denominator and numerator are parallel in the complex plane, so the following conditional expression is obtained:

$$\det\begin{bmatrix}\mathrm{Re}[-(\Delta G)^2] & \mathrm{Re}[(1+G_{uu})(1+G_{dd})]\\ \mathrm{Im}[-(\Delta G)^2] & \mathrm{Im}[(1+G_{uu})(1+G_{dd})]\end{bmatrix} = 0. \tag{24}$$

Substitute ΔG, G_{uu}, and G_{dd} into κ and J_{ij}, and then we get the relation under EP conditions:

$$(J_{uu}+J_{dd})\kappa^2 + 2\kappa + (J_{uu}+J_{dd}) = 0. \tag{25}$$

By solving Eq. (25) for κ and choose a physical solution $\kappa \ll 1$, then we obtain the relationship for $\Delta\varepsilon_{\mathrm{r}}$ and $\Delta\varepsilon_{\mathrm{i}}$ at EP, which is the condition we are looking for:

$$\Delta\varepsilon_{\mathrm{r}} = -\frac{1-\sqrt{1-(I_{uu}+I_{dd})^2(\Delta\varepsilon_{\mathrm{i}})^2}}{I_{uu}+I_{dd}}. \tag{26}$$

Here we numerically verify the EP smoothing and restoration by adjusting the real part of the permittivity. Figure 4(b) shows the band dispersion when the imaginary part of the permittivity is $\Delta\varepsilon_i(r) = -0.2$ only for $y<0$. It reveals that the EPs are smoothed out unlike the case in Fig. 4(a). In this case, $(1+G_{uu})(1+G_{dd})$ is a complex number and EP does not exist in real δk_x space. According to Eq. (26), $\Delta\varepsilon_{\mathrm{r}} = -0.00235$ for $y<0$ is required to cancel the effects of complex coupling in the case of Fig. 4(b) with $\Delta\varepsilon_{\mathrm{i}} = -0.2$ for $y<0$. Figure 4(c) shows the band dispersion when $\Delta\varepsilon_{\mathrm{r}} = -0.00235$ for $y<0$ is introduced, and the EP smoothing is clearly suppressed compared to Fig. 4(b). Thus, even when the EP is smoothed out by the gain-loss imbalance, appropriate adjustment of the real part of the permittivity offsets the complex coupling and restores the anomalous dispersion. In this way, even for modes in photonic crystal waveguides, where a formalism like tight binding is not well known, the effective Hamiltonian model can elucidate the conditions for EP restoration in nontrivial gain-loss imbalance scenarios.

IV. SUPERLUMINAL EDGE STATES AND ENLARGED PROPAGATION LENGTH ON PHOTONIC CRYSTAL WAVEGUIDE

The anomalous dispersion near the EPs leads to the high group velocity of the edge states, which allows the realization of superluminal propagation. Here we numerically verify the

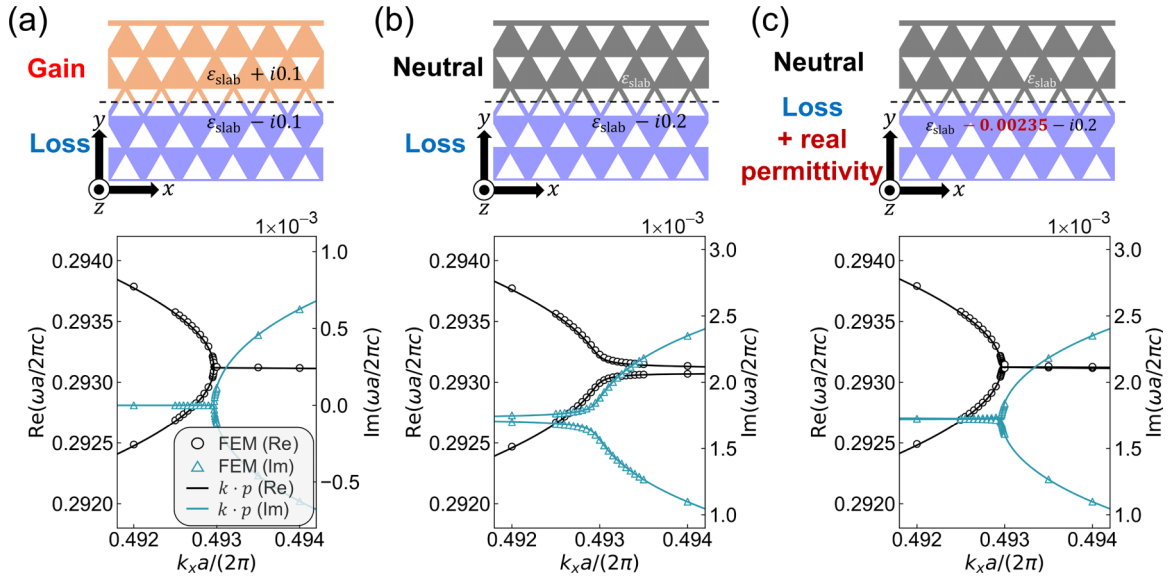

FIG. 4. Comparison of the band dispersion with the FEM calculation and the $\boldsymbol{k} \cdot \boldsymbol{p}$ Hamiltonian. The black circle and blue triangle points represent the real and imaginary parts of the eigenvalues obtained by FEM, while the black and blue lines represent the real and imaginary parts by the $\boldsymbol{k} \cdot \boldsymbol{p}$ Hamiltonian. (a) $\mathcal{PT}$-symmetric permittivity perturbation with $\Delta\varepsilon = i0.1$ for $y > 0$ and $\Delta\varepsilon = -i0.1$ for $y < 0$. (b) $\Delta\varepsilon = -i0.2$ only for $y < 0$. (c) $\Delta\varepsilon = -0.00235 - i0.2$ only for $y < 0$.

group velocity of the edge states, and show that the singularity in the band dispersion near the EP is restored by the method we proposed in the previous section, resulting in a group velocity exceeding the light speed in vacuum c. In addition, we discuss the fast-light effect on the propagation length of the edge states. The propagation length of the edge mode is limited by the lifetime of the edge states in the passive systems, but is expected to increase as the group velocity increases. In the following sections, we will also discuss the expected increase in propagation length based on the anomalous group velocity near the EPs.

The group velocity in non-Hermitian periodic systems was given by the derivative of the real part of the eigenfrequency ω_R with respect to the wave vector k_x, which is consistent with the definition in Ref. [27]:

$$v_g = \left| \frac{\partial \omega_R}{\partial k_x} \right|. \tag{27}$$

Figure 5(a) shows the group velocity of the edge states, which is calculated by the slope of the band dispersion in Fig. 4.

(1) Without permittivity adjustment

(2) With $\Delta\varepsilon = i0.1$ for $y > 0$ and $\Delta\varepsilon = -i0.1$ for $y < 0$ (balanced loss-gain)

(3) With $\Delta\varepsilon = -i0.2$ for $y > 0$

(4) With $\Delta\varepsilon = -0.00235 - i0.2$ for $y < 0$

Here (2), (3), and (4) represent the cases in Figs. 4(a)–4(c), respectively. When the permittivity is not adjusted (1), the maximum group velocity of the edge states is $v_g = 0.17c$. Note that the initial group velocity is larger than that of CROW ($v_g = 0.02c$ in Ref [29]). Then, the group velocity is increased by the balanced loss-gain perturbation $\Delta\varepsilon = \pm i0.1$ (2). The maximum group velocity of the edge states reaches the superluminal ($v_g = 4.5c$), which is determined by the finite mesh of the wave vector Δk_x in the FEM calculation and should theoretically diverge at the EPs. Graph (III) in Fig. 4(a) shows the group velocity of the edge states with loss-biased perturbation $\Delta\varepsilon = -i0.2$ for $y > 0$. The maximum group velocity near the EPs in FEM calculation is subluminal ($v_g = 0.85c$), which is 5.0 times larger than that of $\Delta\varepsilon = 0$ ($v_g = 0.17c$), but is limited by the EP smoothing. The graph (IV) in Fig. 5(a) shows the group velocity of the edge states with the permittivity adjustment $\Delta\varepsilon = -0.00235 - i0.2$ for $y < 0$. The adjustment of the real part of the permittivity restore the EP, and the maximum group velocity of the edge states is accelerated to $v_g = 2.8c$, which is 16.9 times larger than that of $\Delta\varepsilon = 0$. The group velocity calculated from the FEM method is sufficiently close to the singularity predicted by the $\boldsymbol{k} \cdot \boldsymbol{p}$ method. Consequently, by restoring the EP through adjustment of the real part of the permittivity, the group velocity can be increased from subluminal to superluminal.

Since the photon lifetime determined by the absorption is independent of the group velocity, the propagation length of the edge states is expected to increase as the group velocity increases. The propagation length of the edge state l is defined as the length at which the intensity of the light decreases to $1/e$:

$$l = \left| \frac{\partial \omega_R}{\partial k_x} \right| \frac{1}{2\omega_I}, \quad \omega_I > 0. \tag{28}$$

Here ω_R and ω_I are the real and imaginary parts of the eigenfrequency. We only deal with the loss-biased situation $\omega_I > 0$. Figure 5(b) shows the propagation length of the edge states. Here the case with balanced loss-gain perturbation [Fig. 4(a)] is not shown since the propagation length is infinite due to the negative imaginary part of the eigenfrequency. The maximum propagation length is 20 μm when the permittivity adjustment $\Delta\varepsilon = -i0.2$ for $y > 0$ is introduced. Moreover, the propagation length reaches 62 μm with the real part of permittivity adjustment $\Delta\varepsilon = -0.00235 - i0.2$ for $y < 0$, which is due to the suppression of the EP smoothing. The enlarged propaga-

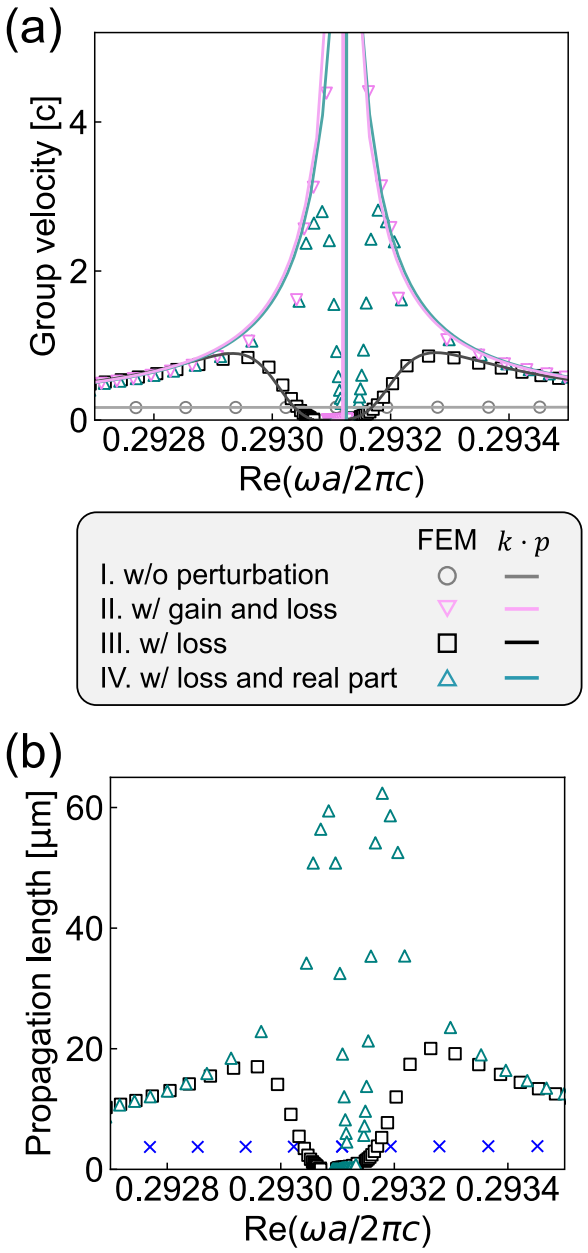

FIG. 5. (a) Group velocity of the edge states in the photonic crystal heterostructure (I) without permittivity adjustment, (II) with $\Delta\varepsilon = i0.1$ for $y > 0$ and $\Delta\varepsilon = -i0.1$ for $y < 0$ (balanced loss-gain), (III) with $\Delta\varepsilon = -i0.2$ for $y > 0$, and (IV) with $\Delta\varepsilon = -0.00235 - i0.2$ for $y < 0$. (II), (III), and (IV) represent the cases in Figs. 4(a)–4(c), respectively. (b) Propagation length of the edge states in the FEM calculation in (III) and (IV). The blue cross denotes with initial permittivity and the same lifetime of the edge states at $k_x a/(2\pi) = 0.49$ in (a) (III).

tion length despite a short lifetime ($\tau := 1/(2\omega_I) = 0.072$ ps) is achieved by the high group velocity effect near the EPs. Assuming the same group velocity in the unperturbed case and the same lifetime at EP for the perturbed cases [IV in Fig. 5(a)], the propagation length is limited to 4.0 μm. In this way, the propagation length of the edge states can be enlarged even in the lossy system, which may allow us to utilize the guided mode even in the passive system.

V. IMPLEMENTATION INTO THE GRAPHENE-LOADED PHOTONIC CRYSTAL SLAB

Our scheme for generating and restoring EPs in photonic crystal waveguides can be applied to the realistic silicon photonic crystal slabs. In this section, we show how to implement our scheme into the graphene-loaded photonic crystal slab. Figure 6(a) shows a schematic of the graphene-loaded photonic crystal slab. We assume the lattice constant is $a = 470$ nm, and the one side of triangular hole is $s = 0.8a$, which is the same as the previous 2D simulations in Fig. 1(a). The thickness of the slab is set to $h = 200$ nm, and the permittivity of the slab is set to $\varepsilon_{\text{slab}} = (3.48)^2$. Then, the 5-sheet of graphene is placed on the top of the slab and one side of the heterostructures ($y < 0$) to generate the EPs. Graphene has remarkable properties for applications in optical devices, such as large absorption in one place and reconfigurable conductivity [42]. It is well known that the optical absorption of graphene depends on its Fermi level, which can be controlled by voltage injection [43–47]. Our choice of graphene in this study is based solely on its ability to easily induce material absorption in photonic crystals, but the graphene has other advantages, such as the ability to reconfigurably control its permittivity. Now we aim to purely perturb the imaginary part of the permittivity since the large real part of the permittivity breaks the EP condition, and graphene is particularly well suited for perturbing only the imaginary part of the permittivity, as it has a large imaginary part of the permittivity in the near-infrared region [48]. In addition, some previous reports have demonstrated the successful loading and precise patterning of graphene onto photonic crystal structures [49,50], further supporting its feasibility for our purposes. We have assumed that the conductivity of graphene is $\sigma = (6.0882 + i0.1908) \times 10^{-5}$ [S/m] per sheet, which is the value from the theoretical formula derived from the Kubo formula [48] with the relaxation time $\tau = 100$ fs, the temperature of graphene $T = 300$ K, the angular frequency of light $\omega = 2\pi c/\lambda$, $\lambda = 1550$ nm, and the Fermi energy of graphene $E_F = 0.2$ eV. The real and imaginary parts of the conductivity correspond to the imaginary and real parts of the permittivity, respectively. See Appendix E for the effect of the misalignment of the graphene sheet.

Figure 6(b) shows the band dispersion of the photonic crystal slab without graphene, and we can see that the linear dispersion of edge states appears near $k_x = \pi/a$ as in the case in Fig. 1(b). Here we focus on two eigenmodes at the Dirac point ($k_x = \pi/a$), and the modes localized at the top and bottom are named modes u and d, the same as the case in Fig. 3(b). The adjustment of the real part of the permittivity for one side of the heterostructure ($y < 0$) as shown in the right panel of Fig. 4(a) can be replaced by the position shift of triangular holes. We choose the triangular hole position in the forth row from the glide symmetry plane to introduce just the right amount of adjustment, as shown by the yellow triangles in Fig. 6(a). Figure 6(c) shows the frequency of the two eigenmodes at $k_x = \pi/a$ without graphene as a function of the y-directional triangular hole shift Δy_{hole}. The frequency of two modes is degenerated in $\Delta y_{\text{hole}} = 0$. The positive hole shift Δy_{hole} perturbs only the mode d, leads to decrease the difference of frequency between two modes, and minimizes

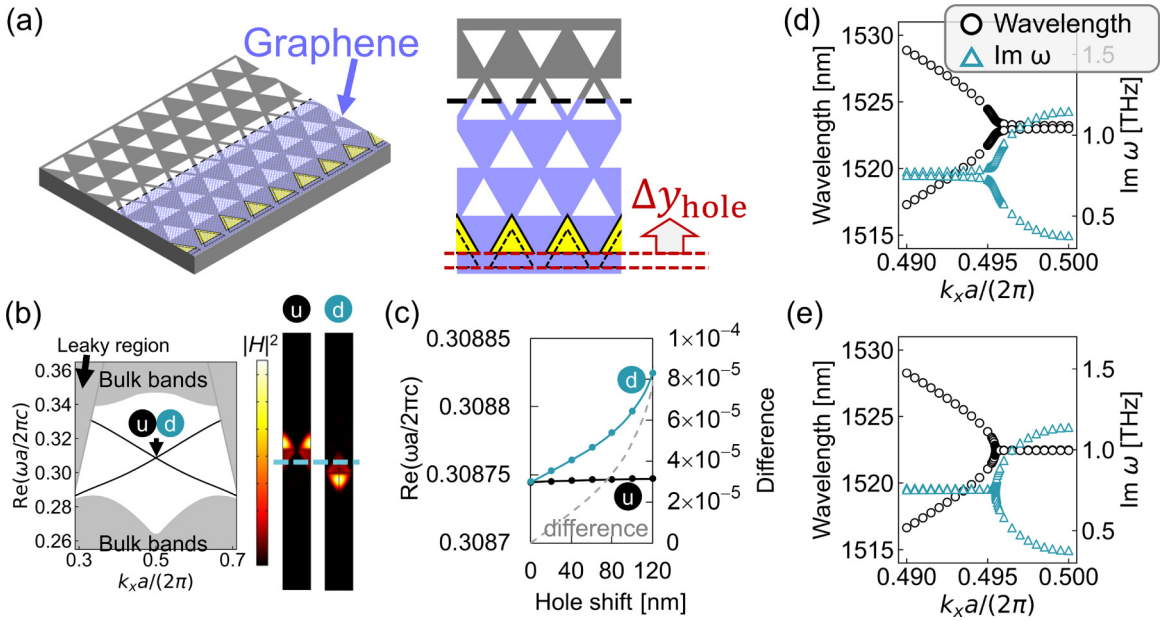

FIG. 6. (a) Schematic of the photonic crystal slab loaded with a 5-sheet of graphene. The right panel describes the hole shift of the position of the triangular hole Δy_{hole}. (b) The band dispersion of the graphene-loaded photonic crystal slab and $|\boldsymbol{H}|^2$ distribution of the eigenmodes at the initial Dirac point. (c) The frequency of the two eigenmodes at $k_x = \pi/a$ without graphene as a function of the triangular hole shift Δy_{hole}. (d), (e) The band dispersion of the graphene-loaded photonic crystal slab (d) without no hole shift and (e) with the hole shift $\Delta y_{\text{hole}} = 104$ nm.

near $\Delta y_{\text{hole}} = 104$ nm. Therefore, the hole shift of the triangular hole can be used to adjust the effective real part of the permittivity. Details are shown in Appendix D.

Next, we investigate the effect of the graphene loading on the band dispersion. Figure 6(d) shows the band dispersion near $k_x = \pi/a$ of the graphene-loaded photonic crystal slab without the triangular hole shift ($\Delta y_{\text{hole}} = 0$). The EPs is smoothed out by the graphene loading, which is not only due to the imaginary coupling in loss-biased system, but also due to the positive permittivity modulation by the graphene sheet. Figure 6(e) shows the band dispersion with the triangular hole shift $\Delta y_{\text{hole}} = 104$ nm. The proper adjustment of triangular holes cancels the contribution of both the imaginary coupling and the imaginary part of conductivity, and restores EP. Consequently, our scheme for generating and restoring EPs in photonic crystal waveguides can be applied to the silicon photonic crystal slabs by loading graphene and adjusting the position of triangular holes.

Finally, we investigate the group velocity of the edge state and corresponding propagation length in some triangular hole shift Δy_{hole}. Figure 7(a) shows the group velocity v_g of the edge states in the graphene-loaded photonic crystal slab near EPs with some triangular hole shift Δy_{hole}. The group velocity of initial photonic crystal waveguide near the Dirac cone is about $v_g = 0.13c$ and increases to $v_g = 0.38c$ when graphene is loaded. However, without the hole shift, the effect of the EP smoothing strongly limits the peak of group velocity. When a hole shift is added, the EP smoothing gradually mitigates and the group velocity peak is maximized around $\Delta y_{\text{hole}} = 104$ nm. A series of changes in the group velocity with Δy_{hole} correspond to the change of frequency difference at $k_x a = \pi$ between the two modes provided by the hole shift, as shown in Fig. 6(d). The group velocity reaches $v_g = 3.3c$ near the restored EPs in the case of $\Delta y_{\text{hole}} = 104$ nm, and is accelerated to 25 times of that without graphene. The bandwidth where the group velocity is accelerated over the speed of light in vacuum is up to 0.4 nm as shown in Fig. 7(a), which corresponds to 1.5 ps in terms of time width assuming a Gaussian pulse. Importantly, the propagation length is also elongated by the same ratio, directly resulting from the fast light effect. We confirmed that the propagation length l is elongated to 105 μm near the restored EPs as shown in Fig. 7(b), which is a staggering number for a lifetime of 0.11 ps. It takes 0.38 ps to propagate the same distance in air, and it is expected that this difference can be detected for a pulse length of 1.5 ps, given the ratio of pulse length to group delay $(0.38 - 0.11)/1.5 \approx 0.18$: This value is better than the previously reported ratio of pulse width to group delay in superluminal propagation experiments $(23.8\ \mu\text{s})/(0.05\ \text{s}) \approx 0.048$ [23]. In addition, the group velocity of the edge state in a photonic crystal waveguide without graphene is about one-seventh of that in air, making it even easier to measure the difference in group delay.

For practical measurements, group delay measurements as described in Ref. [22] is considered. As mentioned above, the required time resolution is reasonable compared to the previous superluminal experiments. Furthermore, the graphene's properties in our simulation are realistic, and the precision of the triangular hole shifts is within the resolution of the electron beam lithography. The effect of graphene misalignment is also discussed in Appendix E. Therefore, the parameters required for superluminal propagation in our structure are realistic. Alternatively, instead of group delay measurements, the superluminal state could be indirectly observed by visualizing the photonic band structure through reflection measurements [51,52]. However, since the EP is below the light line, additional techniques such as the introduction of a perturbation as described in [53] are required.

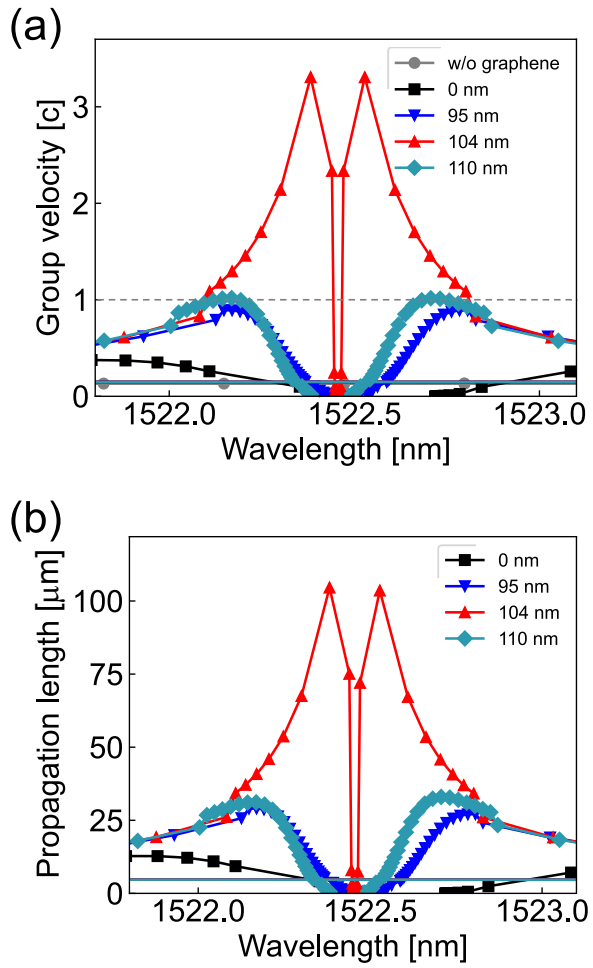

FIG. 7. (a) Group velocity v_g and (b) Propagation length l of the edge states in the graphene-loaded photonic crystal slab near EPs.

VI. CONCLUSION

We have proposed a feasible photonic crystal waveguide for realizing superluminal edge states. A systematic method to produce EPs in non-Hermitian photonic crystal waveguides with glide and time-reversal symmetry has been presented, and the exact EP condition about the permittivity adjustment is analytically derived by $\boldsymbol{k} \cdot \boldsymbol{p}$ Hamiltonian. We have shown that the EPs can be generated by introducing the loss bias to the system, and the EPs can be restored by appropriately adjusting the permittivity. The anomalous dispersion near the EPs leads to the high group velocity of the edge states, which allows the realization of superluminal propagation. In addition, the high group velocity of the edge states near the EPs enlarges the propagation length of the waveguide, even in the lossy and short lifetime system. We have confirmed that the group velocity contrast of the edge state is increased and corresponding propagation length is enlarged by appropriately adjusting the permittivity to restore EP. Our scheme for generating and restoring EPs in photonic crystal waveguides can be applied to the silicon photonic crystal slabs by loading graphene and adjusting the position of triangular holes. We have confirmed that the group velocity v_g is accelerated to 25 times of that without graphene near the restored EPs, thereby realizing the superluminal edge state ($v_g = 3.3c$). Importantly, the propagation length is also elongated by the same ratio, directly resulting from the fast light effect.

Our study paves the way to realize the observation of superluminal propagation states in photonic crystal waveguide. The fast-light on-tip nanodevices have the potential for the development of control of light-matter interaction as well as the traditional slow-light waveguide, opening up new possibilities for the application of optical computing. In addition, the proposed method for generating and restoring EPs in photonic crystal waveguides will be useful for the development of non-Hermitian photonic devices. Furthermore, in addition to the anomalous dispersion in the edge states, our structure has an additional intriguing aspect about the topological properties. The proposed structure is based on a photonic crystal waveguide, known for exhibiting edge states with valley-polarized characteristics and robustness against bending [20,54]. Our structure involves uniform permittivity perturbations on both sides of a glide plane, which preserves the symmetry of the effective Hamiltonian for the bulk. This results in maintaining a finite Berry curvature near the K and K′ points in the band structure. Consequently, the edge states near the EPs retain valley-polarized topological features. Although a detailed discussion of valley topology is beyond the scope of this work, our proposed structure holds potential for application in valley photonic devices, and provides a pathway for developing innovative photonic devices.

ACKNOWLEDGMENTS

This work was supported by the Japan Society for the Promotion of Science (Grants No. JP20H05641, No. JP21K14551, No. 24K01377, No. 24H02232, and No. 24H00400).

DATA AVAILABILITY

Data underlying the results presented in this paper are not publicly available at this time but may be obtained from the authors upon reasonable request.

APPENDIX A: THE DESIGN OF HETEROSTRUCTURE IN OTHER LATTICE OR HOLE SHAPES

Our scheme for generating EPs from a symmetry-oriented Dirac point can be applied to other lattice structures and hole shapes as long as the spatial photonic crystal geometry has the glide symmetry. Figure 8(a) shows the schematic and the band dispersion in the honeycomb lattice photonic crystal. The slab permittivity and the amount of the perturbation are the same as in the triangular lattice. It is obvious that the EPs generated by the non-Hermitian perturbation on both sides of the glide plane are the same as in the triangular lattice. On the other hand, the generated EPs are outside the band gap when we adopt the honeycomb lattice, and it is difficult to bring the EPs inside the band gap by some kind of tuning. Figure 8(b) shows the results when we adopt the triangular lattice with a circular hole, and there is no significant difference compared with the use of triangular holes. Thus, our proposed method for generating symmetry-oriented EPs can be applied to photonic crystal with different lattice structures. The structure of the triangular lattice and triangular holes shown in Fig. 1 will be

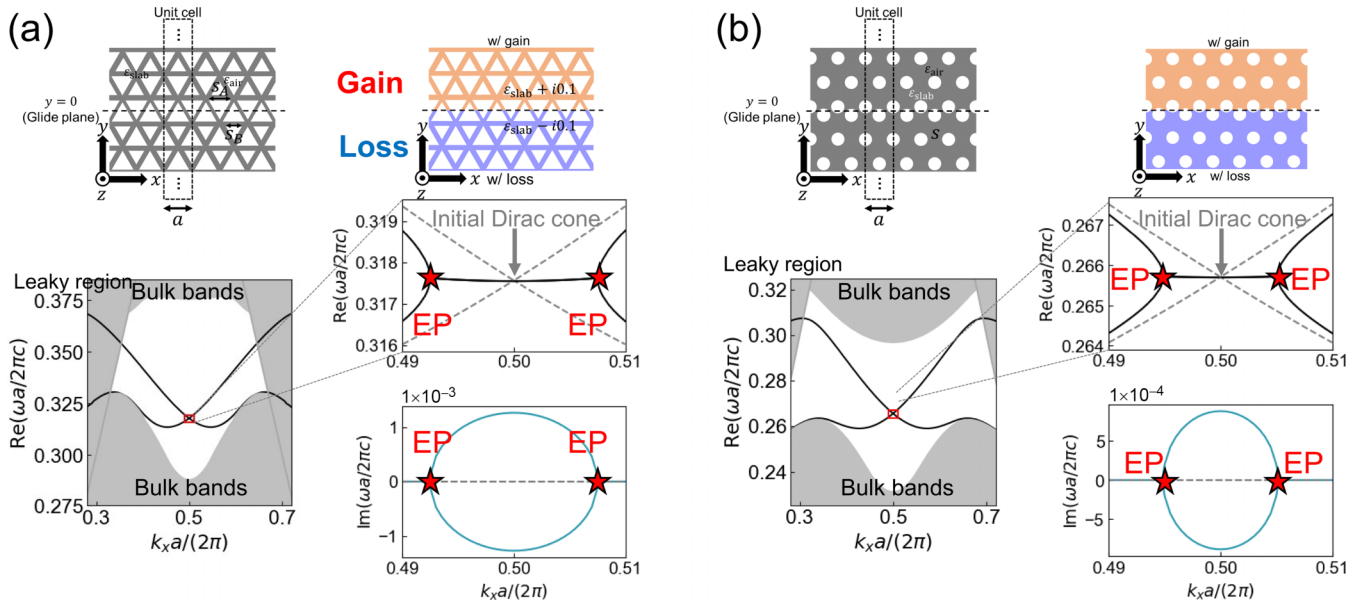

FIG. 8. Interface geometry and band dispersion curves of the photonic crystal heterostructure with (a) the honeycomb lattice and triangular holes, and (b) the triangular lattice and circular holes.

analyzed in the following Appendix because it is suitable for fast-light waveguide applications since the EP is inside the band gap, the band slope (group velocity) near the Dirac point is large, and the band gap is wide.

APPENDIX B: H_z DISTRIBUTION OF THE EIGENMODES

In the context of a two-band system with $\mathcal{PT}$ symmetry, the phase transition of eigenvalues and eigenstates through the EP is known as the $\mathcal{PT}$ phase transition [5]. Since we now focus on the TE mode, the two eigenmodes are characterized by their H_z distributions. For three points, namely, outside the EP ($k_x = 0.49 \times 2\pi/a$), at the EP ($k_x = 0.49297 \times 2\pi/a$), and at the original Dirac point ($k_x = \pi/a$), we present the H_z distributions of the two bands at each k_x point in Fig. 9. We discuss the presence or absence of $\mathcal{PT}$ symmetry for each case. At $k_x = 0.49 \times 2\pi/a$, the H_z distribution is symmetric about $y = 0$, which is consistent with both eigenvalues being real. In addition, the symmetry under simultaneous space and time-reversal operations, i.e., $(\hat{G}\hat{T})H_z^{(i)} = H_z^{(i)}$ and $i = 1, 2$ denotes the label of eigenmodes, is evident from the figure ($\mathcal{PT}$-symmetric phase). Similar features are observed in the EP ($k_x = 0.49297 \times 2\pi/a$), but the two eigenmodes show complete coalescence, which distinguishes it from the $k_x = 0.49 \times 2\pi/a$ case. At $k_x = \pi/a$, the H_z distribution under $\mathcal{PT}$ operations is no longer symmetric but shows an asymmetric distribution with one side favoring gain and the other side favoring loss ($\mathcal{PT}$-broken phase). In summary, the H_z distributions of the eigenmodes in the heterostructure shown in Fig. 1 satisfy the properties of a general $\mathcal{PT}$-symmetric system.

APPENDIX C: DERIVATION OF THE $\boldsymbol{k}\cdot\boldsymbol{p}$ HAMILTONIAN

Here we derive the $\boldsymbol{k}\cdot\boldsymbol{p}$ Hamiltonian from the Maxwell's equations. The details of the derivation are shown in Ref. [41].

The Maxwell's equations in the photonic crystal are given by [55]

$$\nabla \times \nabla \times \boldsymbol{E}_{nk}(\boldsymbol{r}) = [\varepsilon(\boldsymbol{r}) + \Delta\varepsilon(\boldsymbol{r})]\left(\frac{\omega_{nk}}{c}\right)^2 \boldsymbol{E}_{nk}(\boldsymbol{r}). \quad \text{(C1)}$$

Here $\varepsilon(\mathbf{r})$ is the permittivity of initial photonic crystal, and $\Delta\varepsilon(\mathbf{r}) := \Delta\varepsilon_{\mathbf{r}} + i\Delta\varepsilon_{\mathbf{i}}(\mathbf{r})$ is the perturbation of the permittivity. ω_{nk} and $\boldsymbol{E}_{nk}(\boldsymbol{r})$ are the eigenfrequency and electric

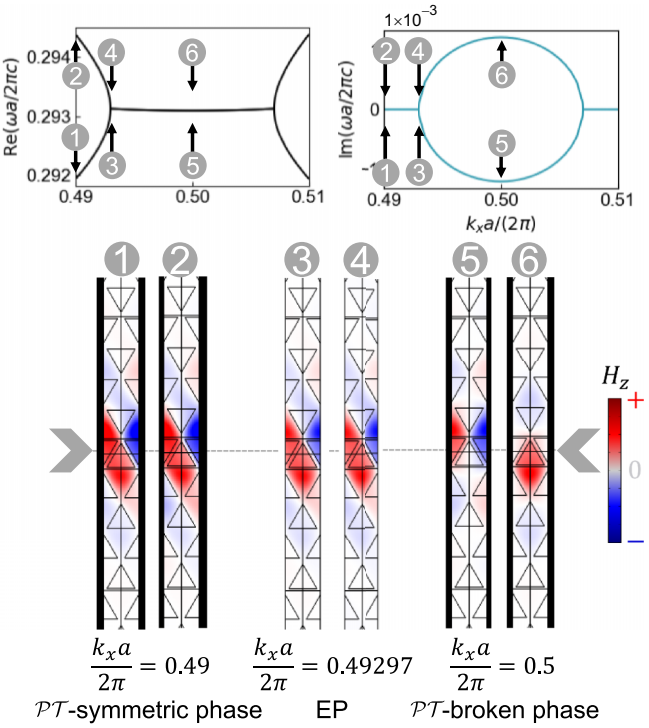

FIG. 9. H_z distribution of the eigenmodes in the photonic crystal heterostructure at (a) $k_x a/(2\pi) = 0.49$, (b) 0.49297 (EP), and (c) 0.5.

field profile of the photonic crystal, respectively, and $\omega_n^{(0)}$ is the unperturbed eigenfrequency. Let $U_n^{(0)}$ be the unperturbed eigenenergy, and the bases $\boldsymbol{E}_{nk}^{(0)}(\boldsymbol{r})$ hold the orthonormality condition:

$$\frac{\varepsilon_0}{4}\int_{\text{u.c.}} \varepsilon(\boldsymbol{r})\boldsymbol{E}_{nk}^{(0)*}(\boldsymbol{r})\cdot\boldsymbol{E}_{mk}^{(0)}(\boldsymbol{r})\,\mathrm{d}\boldsymbol{r} = U_n^{(0)}\delta_{nm}. \tag{C2}$$

Then we define the normalized eigenmodes $\boldsymbol{\psi}_{nk}^{(0)}(\boldsymbol{r})$ as

$$\boldsymbol{\psi}_{nk}^{(0)}(\boldsymbol{r}) = \frac{\sqrt{\varepsilon_0}}{2\sqrt{U_n^{(0)}}}\boldsymbol{E}_{nk}^{(0)}(\boldsymbol{r}), \tag{C3}$$

and we get the following equation:

$$\nabla\times\nabla\times\boldsymbol{\psi}_{nk}(\boldsymbol{r}) = [\varepsilon(\boldsymbol{r})+\Delta\varepsilon(\boldsymbol{r})]\left(\frac{\omega_{nk}}{c}\right)^2\boldsymbol{\psi}_{nk}(\boldsymbol{r}), \tag{C4}$$

$$\int_{\text{u.c.}} \varepsilon(\boldsymbol{r})\boldsymbol{\psi}_{nk}^{(0)*}(\boldsymbol{r})\cdot\boldsymbol{\psi}_{mk}^{(0)}(\boldsymbol{r})\,\mathrm{d}\boldsymbol{r} = \delta_{nm}. \tag{C5}$$

Like the electric field, the magnetic field is also normalized as

$$\boldsymbol{\varphi}_{nk}^{(0)}(\boldsymbol{r}) = \frac{\sqrt{\mu_0}}{2\sqrt{U_n^{(0)}}}\boldsymbol{H}_{nk}^{(0)}(\boldsymbol{r}). \tag{C6}$$

Next, we expand the wave function $\boldsymbol{\psi}_{nk}(\boldsymbol{r})$ when $\Delta\varepsilon(\boldsymbol{r})$ is finite by the wave function at $\boldsymbol{k} = [k_0, 0, 0]^\top$, $k_0 = \pi/a$ with $\Delta\varepsilon(\boldsymbol{r}) = 0$:

$$\boldsymbol{\psi}_{nk}(\boldsymbol{r}) = \sum_j C_{nj}(k)e^{i\delta\boldsymbol{k}\cdot\boldsymbol{r}}\boldsymbol{\psi}_{jk_0}^{(0)}(\boldsymbol{r}). \tag{C7}$$

Here $\delta\boldsymbol{k} = \boldsymbol{k} - [k_0, 0, 0]^\top$ and $C_{nj}(k)$ is the expansion coefficient. Substitute Eq. (C7) into Eq. (C4), and we get

$$\begin{aligned}
&\sum_j C_{nj}(k)e^{i\delta\boldsymbol{k}\cdot\boldsymbol{r}}A\boldsymbol{\psi}_{jk_0}^{(0)}(\boldsymbol{r}) \\
&= \left(\frac{\omega_{nk}}{c}\right)^2[\varepsilon(\boldsymbol{r})+\Delta\varepsilon(\boldsymbol{r})]\sum_j C_{nj}(k)e^{i\delta\boldsymbol{k}\cdot\boldsymbol{r}}\boldsymbol{\psi}_{jk_0}^{(0)}(\boldsymbol{r}), \\
A &:= -\delta\boldsymbol{k}\times(\delta\boldsymbol{k}\times) + i(\nabla\times(\delta\boldsymbol{k}\times)) \\
&\quad + i(\delta\boldsymbol{k}\times(\nabla\times)) + \nabla\times(\nabla\times).
\end{aligned} \tag{C8}$$

Furthermore, by multiplying from the left by $e^{-i\delta\boldsymbol{k}\cdot\boldsymbol{r}}\boldsymbol{\psi}_{ik_0}^{(0)*}(\boldsymbol{r})$ and integrating over the unit cell, the eigenvalue equation determining the band structure is obtained:

$$\begin{aligned}
&\sum_j\left[\left(\frac{\omega_{jk}^{(0)}}{c}\right)^2\delta_{ij} + P'_{ij} + Q'_{ij}\right]C_{nj}(k) \\
&= \left(\frac{\omega_{nk}}{c}\right)^2\sum_j(\delta_{ij}+G_{ij}).
\end{aligned} \tag{C9}$$

Here $\nabla\times\nabla\times\boldsymbol{\psi}_{jk}^{(0)}(\boldsymbol{r}) = \varepsilon(\boldsymbol{r})\left(\frac{\omega_{nk}^{(0)}}{c}\right)^2\boldsymbol{\psi}_{jk}^{(0)}(\boldsymbol{r})$ is used in the derivation. P'_{ij}, G_{ij}, Q'_{ij} are defined as follows:

$$\begin{aligned}
P'_{ij} &= \int_{\text{u.c.}}\left[\omega_j^{(0)}\boldsymbol{\psi}_{ik_0}^{(0)*}(\boldsymbol{r})\times\boldsymbol{\varphi}_{jk_0}^{(0)}(\boldsymbol{r})\right. \\
&\quad \left. - \omega_i^{(0)}\boldsymbol{\varphi}_{ik_0}^{(0)*}(\boldsymbol{r})\times\boldsymbol{\psi}_{jk_0}^{(0)}(\boldsymbol{r})\right]\cdot\delta\boldsymbol{k}\,\mathrm{d}^3r \\
&=: \boldsymbol{P}_{ij}\cdot\delta\boldsymbol{k},
\end{aligned} \tag{C10}$$

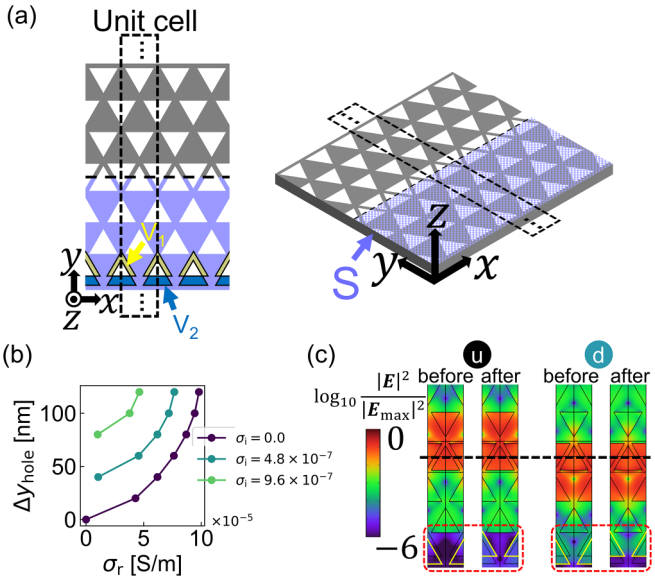

FIG. 10. (a) The definition of the domain V_1, V_2 and the surface S. (b) The required triangular hole shift Δy_{hole} to restore the EPs as a function of a real part of conductivity σ_r at each imaginary part of conductivity σ_i [S/m]. (c) The electric field distribution of the eigenmodes at $k_x = \pi/a$ before and after the hole shift.

$$G_{ij} = \int_{\text{u.c.}}\Delta\varepsilon(\boldsymbol{r})\boldsymbol{\psi}_{ik_0}^{(0)*}(\boldsymbol{r})\cdot\boldsymbol{\psi}_{jk_0}^{(0)}(\boldsymbol{r})\,\mathrm{d}^3r, \tag{C11}$$

$$\begin{aligned}
Q'_{ij} &= -\int_{\text{u.c.}}\boldsymbol{\psi}_{ik_0}^{(0)*}(\boldsymbol{r})\cdot\left[\delta\boldsymbol{k}\times\delta\boldsymbol{k}\times\boldsymbol{\psi}_{jk_0}^{(0)}(\boldsymbol{r})\right]\mathrm{d}^3r \\
&= (\delta k_x)^2\int_{\text{u.c.}}\left\{\left[\psi_{ik_0}^{(0)*}(\boldsymbol{r})\right]_y\left[\psi_{jk_0}^{(0)}(\boldsymbol{r})\right]_y\right. \\
&\quad \left. + \left[\psi_{ik_0}^{(0)*}(\boldsymbol{r})\right]_z\left[\psi_{jk_0}^{(0)}(\boldsymbol{r})\right]_z\right\}\mathrm{d}^3r \\
&=: (\delta k_x)^2 Q_{ij}.
\end{aligned} \tag{C12}$$

APPENDIX D: THE EP CONDITION WITH THE HOLE SHIFT IN $\boldsymbol{k}\cdot\boldsymbol{p}$ HAMILTONIAN

We have shown in Sec. III B of that the EP can be restored by appropriately adjusting the real part of the permittivity, and adopted the shift of the triangular holes in the realistic structure as a method instead of the permittivity adjustment in Appendix E. Here we theoretically investigate the effect of the triangular hole shift and show that the triangular hole shift offsets the effect of the permittivity adjustment.

The following describes the setup for treating the triangular hole shift and graphene loading as perturbations in the permittivity. A domain V_1, V_2 and surface S are defined as shown in Fig. 10(a). The domain V_1, V_2 is defined as the regions where the permittivity changes from silicon to air and from air to silicon, respectively, when the triangular holes are shifted by Δy_{hole}. Moreover, the surface S is defined as the region where the graphene is loaded. The elements of the matrix G defined by Eq. (6) are the sum of the contributions from the domains

V_1, V_2 and the surface S as follows:

$$G_{\alpha\beta} = G_{\alpha\beta}^{(V_1)} + G_{\alpha\beta}^{(V_2)} + G_{\alpha\beta}^{(S)}, \quad \alpha, \beta = \mathrm{d}, \mathrm{u}. \tag{D1}$$

Here $G_{\mathrm{ud}}, G_{\mathrm{du}}$ are zero because all the domains and surfaces have mirror symmetry with respect to the y axis of the unit cell. The contributions from the domains V_1, V_2 are given by

$$G_{\alpha\beta}^{(V_1)} = (\varepsilon_{\mathrm{air}} - \varepsilon_{\mathrm{slab}}) \int_{V_1} \boldsymbol{\psi}_{\alpha k_0}^{(0)*}(\boldsymbol{r}) \cdot \boldsymbol{\psi}_{\beta k_0}^{(0)}(\boldsymbol{r})\, \mathrm{d}^3 r, \tag{D2}$$

$$G_{\alpha\beta}^{(V_2)} = (\varepsilon_{\mathrm{slab}} - \varepsilon_{\mathrm{air}}) \int_{V_2} \boldsymbol{\psi}_{\alpha k_0}^{(0)*}(\boldsymbol{r}) \cdot \boldsymbol{\psi}_{\beta k_0}^{(0)}(\boldsymbol{r})\, \mathrm{d}^3 r. \tag{D3}$$

The permittivity of the silicon and air is denoted as $\varepsilon_{\mathrm{slab}}$ and $\varepsilon_{\mathrm{air}}$, respectively. To simplify the notation, we introduce the following quantities:

$$I_{\alpha\beta}^{(V)} = \int_{V} \boldsymbol{\psi}_{\alpha k_0}^{(0)*}(\boldsymbol{r}) \cdot \boldsymbol{\psi}_{\beta k_0}^{(0)}(\boldsymbol{r})\, \mathrm{d}^3 r. \tag{D4}$$

Then the contributions from V_1 and V_2 are collectively denoted as $Y_{\mathrm{d}}, Y_{\mathrm{u}}$:

$$Y_{\mathrm{d}} := G_{\mathrm{dd}}^{(V_1)} + G_{\mathrm{dd}}^{(V_2)} = (\varepsilon_{\mathrm{slab}} - \varepsilon_{\mathrm{air}})\big(I_{\mathrm{dd}}^{(V_2)} - I_{\mathrm{dd}}^{(V_1)}\big), \tag{D5}$$

$$Y_{\mathrm{u}} := G_{\mathrm{uu}}^{(V_1)} + G_{\mathrm{uu}}^{(V_2)} = (\varepsilon_{\mathrm{slab}} - \varepsilon_{\mathrm{air}})\big(I_{\mathrm{uu}}^{(V_2)} - I_{\mathrm{uu}}^{(V_1)}\big). \tag{D6}$$

Next, we consider the contribution from the surface S. Since the complex conductivity of the graphene is given by $\sigma = \sigma_r + i\sigma_i$, the permittivity perturbation due to the graphene loading is given by

$$\Delta\varepsilon(\boldsymbol{r}) = -i\frac{\sigma}{t\omega\varepsilon_0}, \quad \boldsymbol{r} \in S. \tag{D7}$$

Here t is the thickness of the graphene, ω is the angular frequency, and ε_0 is the vacuum permittivity. For simplicity, we will ignore wavelength dispersion of the frequency. Then the contribution from the surface S is given by

$$\begin{aligned} G_{\alpha\beta}^{(S)} &= \int_S \frac{-i\sigma}{t\omega\varepsilon_0} \boldsymbol{\psi}_{\alpha k_0}^{(0)*}(\boldsymbol{r}) \cdot \boldsymbol{\psi}_{\beta k_0}^{(0)}(\boldsymbol{r}) t\, \mathrm{d}^2 r \\ &= -\frac{i\sigma}{\omega\varepsilon_0} \int_S \boldsymbol{\psi}_{\alpha k_0}^{(0)*}(\boldsymbol{r}) \cdot \boldsymbol{\psi}_{\beta k_0}^{(0)}(\boldsymbol{r})\, \mathrm{d}^2 r \\ &=: -i\sigma L_{\alpha\beta}, \end{aligned} \tag{D8}$$

where

$$L_{\alpha\beta} = \frac{1}{\omega\varepsilon_0} \int_S \boldsymbol{\psi}_{\alpha k_0}^{(0)*}(\boldsymbol{r}) \cdot \boldsymbol{\psi}_{\beta k_0}^{(0)}(\boldsymbol{r})\, \mathrm{d}^2 r. \tag{D9}$$

The contributions from the domains V_1, V_2 and the surface S are collectively denoted as

$$G_{\mathrm{dd}} = Y_{\mathrm{d}} + (\sigma_i - i\sigma_r) L_{\mathrm{dd}}, \tag{D10}$$

$$G_{\mathrm{uu}} = Y_{\mathrm{u}} + (\sigma_i - i\sigma_r) L_{\mathrm{uu}}. \tag{D11}$$

All V_1, V_2 and S depend on the hole shift Δy_{hole}, but the value of $L_{\alpha\beta}$ is almost constant since the contribution of the hole shift in the graphene-loaded region is small.

Next, we calculate the components to evaluate the EP condition in Eq. (24):

$$\begin{aligned} 4\Delta G &= G_{\mathrm{dd}} - G_{\mathrm{uu}} \\ &= Y_{\mathrm{d}} - Y_{\mathrm{u}} + (\sigma_i - i\sigma_r)(L_{\mathrm{dd}} - L_{\mathrm{uu}}) \\ &=: \Delta y + (\sigma_i - i\sigma_r)\Delta L, \end{aligned} \tag{D12}$$

$$\begin{aligned} &(1 + G_{\mathrm{dd}})(1 + G_{\mathrm{uu}}) \\ &= (1 + Y_{\mathrm{d}} + \sigma_i L_{\mathrm{dd}} - i\sigma_r L_{\mathrm{dd}})(1 + Y_{\mathrm{u}} + \sigma_i L_{\mathrm{uu}} - i\sigma_r L_{\mathrm{uu}}) \\ &= (1 + Y_{\mathrm{d}} + \sigma_i L_{\mathrm{dd}})(1 + Y_{\mathrm{u}} + \sigma_i L_{\mathrm{uu}}) - \sigma_r^2 L_{\mathrm{dd}} L_{\mathrm{uu}} \\ &\quad - i\sigma_r((1 + Y_{\mathrm{d}} + \sigma_i L_{\mathrm{dd}})L_{\mathrm{uu}} + (1 + Y_{\mathrm{u}} + \sigma_i L_{\mathrm{uu}})L_{\mathrm{dd}}). \end{aligned} \tag{D13}$$

By substituting the above equations into Eq. (24), we obtain the EP condition as follows:

$$\sigma_r^2 = \frac{m^2 l - 2m\Delta L(1 + Y_{\mathrm{d}} + \sigma_i L_{\mathrm{dd}})(1 + Y_{\mathrm{u}} + \sigma_i L_{\mathrm{uu}})}{l(\Delta L)^2 - 2m\Delta L L_{\mathrm{dd}} L_{\mathrm{uu}}}, \tag{D14}$$

where

$$l = (1 + Y_{\mathrm{d}} + \sigma_i L_{\mathrm{dd}})L_{\mathrm{uu}} + (1 + Y_{\mathrm{u}} + \sigma_i L_{\mathrm{uu}})L_{\mathrm{dd}}, \tag{D15}$$

$$m = Y_{\mathrm{d}} - Y_{\mathrm{u}} + \sigma_i \Delta L. \tag{D16}$$

Equation (D14) assures us that the EP can be restored by shifting the triangular holes. From the expression for $Y_{\mathrm{d}} + \sigma_i L_{\mathrm{dd}}$ and $Y_{\mathrm{u}} + \sigma_i L_{\mathrm{uu}}$ that appears in Eq. (D14), it can be seen that the triangular hole shift Δy_{hole} and the imaginary part of the graphene conductivity (i.e., the real part of the permittivity) have the opposite effect on the permittivity perturbation. Generally, $I_{\mathrm{dd}}^{(V_2)} < I_{\mathrm{dd}}^{(V_1)}$, $I_{\mathrm{uu}}^{(V_2)} < I_{\mathrm{uu}}^{(V_1)}$ hold since the edge states are localized near the glide plane. Consequently, $Y_{\mathrm{d}}, Y_{\mathrm{u}}$ defined by Eqs. (D5) and (D6) are negative. Therefore, the triangular hole shift Δy_{hole} has the same effect as a net negative tuning of the real part of the permittivity. Furthermore, due to the difference in the electric field distribution between modes u and d, the permittivity perturbation due to the hole shift affects only the d mode. Note that since graphene has a positive imaginary part of its electrical conductivity, i.e., a positive real part of its permittivity, it is not possible to restore the EP only using graphene.

Figure 10(b) shows the relationship between the real part of the conductivity and the triangular hole shift required to satisfy the EP condition when the imaginary part of the conductivity is fixed. When the imaginary part of the conductivity is zero, the triangular hole shift that satisfies the EP condition is approximately proportional to the square of the real part of the conductivity. As previously mentioned, a positive imaginary part of the conductivity has an opposite effect to the triangular hole shift, so the larger the imaginary part of the conductivity, the narrower the range of the real part of the conductivity that can be canceled out by the triangular hole shift. In practice, the imaginary part of the conductivity for graphene is about $\sigma_i = 2 \times 10^{-6}$ [S/m] [48] so within the range of perturbation theory, it is difficult to restore EP using only the hole shift. In actual FEM calculations, however, the EP restoration has been confirmed with a hole shift of about $\Delta y_{\mathrm{hole}} = 105$ nm, but this is believed to be due to the large permittivity contrast $\varepsilon_{\mathrm{slab}} - \varepsilon_{\mathrm{air}} \approx 11$, which causes changes in the electric field distribution, making the contribution of the actual triangular hole shift larger than the linear perturbation

effect. The change in the electric field distribution due to the triangular hole shift is confirmed in Fig. 10(c).

APPENDIX E: RESTORATION OF EPS AND GROUP VELOCITY IN GRAPHENE-LOADED STRUCTURES WITH MISALIGNMENT

The graphene-loaded structure proposed in this Appendix assumes that graphene is placed along the glide-symmetry plane. From the perspective of fabrication and measurement, it is important to consider the effects on EP and group velocity when the graphene alignment is offset. In practice, even if the graphene position is misaligned, our scheme for EP restoration can still be applied without issue. Figure 11(a) shows the case where the graphene-loading position is shifted by $\sqrt{3}a/4$ below the glide plane. For this structure, the band diagram and group velocity for both the case without triangular hole shifts and with a shift of 44 nm are shown in Figs. 11(b) and 11(c), respectively. As is evident from the figures, even when the graphene position is misaligned, the EP is restored, and the singularity in group velocity is recovered as shown in Fig. 11(d). Mathematically, the misalignment of the graphene-loading position is equivalent to changing the magnitude of graphene's complex permittivity. In other words, it ultimately affects the value of the integral $L_{\alpha\beta}$ in Eq. (D9). Therefore, by adjusting the value of the triangular hole shift or permittivity shift required to cancel the EP, it is possible to restore the EP in exactly the same manner as in the case without misalignment.

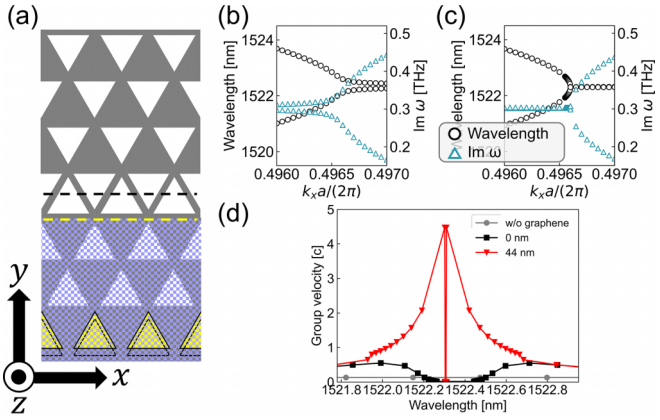

FIG. 11. (a) Schematic of the photonic crystal slab loaded with a 5-sheet of graphene, where the graphene is misaligned by $\sqrt{3}a/4$ below the glide plane (black dashed line). (b), (c) The band dispersion of the photonic crystal slab with the graphene misalignment, (b) without any hole shift and (c) with the hole shift $\Delta y_{\text{hole}} = 44$ nm. (d) The group velocity of the edge states near the EPs with and without the hole shift.

[1] C. M. Bender and S. Boettcher, Real spectra in non-Hermitian Hamiltonians having $\mathcal{PT}$ symmetry, Phys. Rev. Lett. **80**, 5243 (1998).

[2] C. M. Bender, Making sense of non-Hermitian Hamiltonians, Rep. Prog. Phys. **70**, 947 (2007).

[3] M. Parto, S. Wittek, H. Hodaei, G. Harari, M. A. Bandres, J. Ren, M. C. Rechtsman, M. Segev, D. N. Christodoulides, and M. Khajavikhan, Edge-mode lasing in 1D topological active arrays, Phys. Rev. Lett. **120**, 113901 (2018).

[4] K. Takata, K. Nozaki, E. Kuramochi, S. Matsuo, K. Takeda, T. Fujii, S. Kita, A. Shinya, and M. Notomi, Observing exceptional point degeneracy of radiation with electrically pumped photonic crystal coupled-nanocavity lasers, Optica **8**, 184 (2021).

[5] L. Feng, R. El-Ganainy, and L. Ge, Non-Hermitian photonics based on parity–time symmetry, Nat. Photon. **11**, 752 (2017).

[6] A. Regensburger, C. Bersch, M.-A. Miri, G. Onishchukov, D. N. Christodoulides, and U. Peschel, Parity-time synthetic photonic lattices, Nature (London) **488**, 167 (2012).

[7] Ş. K. Özdemir, S. Rotter, F. Nori, and L. Yang, Parity–time symmetry and exceptional points in photonics, Nat. Mater. **18**, 783 (2019).

[8] B. Peng, Ş. K. Özdemir, F. Lei, F. Monifi, M. Gianfreda, G. L. Long, S. Fan, F. Nori, C. M. Bender, and L. Yang, Parity–time-symmetric whispering-gallery microcavities, Nat. Phys. **10**, 394 (2014).

[9] W. Chen, Ş. Kaya Özdemir, G. Zhao, J. Wiersig, and L. Yang, Exceptional points enhance sensing in an optical microcavity, Nature (London) **548**, 192 (2017).

[10] L. Feng, Z. J. Wong, R.-M. Ma, Y. Wang, and X. Zhang, Single-mode laser by parity-time symmetry breaking, Science **346**, 972 (2014).

[11] H. Hodaei, M.-A. Miri, M. Heinrich, D. N. Christodoulides, and M. Khajavikhan, Parity-time-symmetric microring lasers, Science **346**, 975 (2014).

[12] A. Guo, G. J. Salamo, D. Duchesne, R. Morandotti, M. Volatier-Ravat, V. Aimez, G. A. Siviloglou, and D. N. Christodoulides, Observation of $\mathcal{PT}$-symmetry breaking in complex optical potentials, Phys. Rev. Lett. **103**, 093902 (2009).

[13] A. Szameit, M. C. Rechtsman, O. Bahat-Treidel, and M. Segev, $\mathcal{PT}$-symmetry in honeycomb photonic lattices, Phys. Rev. A **84**, 021806(R) (2011).

[14] T. Baba, Slow light in photonic crystals, Nat. Photon. **2**, 465 (2008).

[15] A. Yariv, Y. Xu, R. K. Lee, and A. Scherer, Coupled-resonator optical waveguide: A proposal and analysis, Opt. Lett. **24**, 711 (1999).

[16] S. Olivier, C. Smith, M. Rattier, H. Benisty, C. Weisbuch, T. Krauss, R. Houdré, and U. Oesterlé, Miniband transmission in a photonic crystal coupled-resonator optical waveguide, Opt. Lett. **26**, 1019 (2001).

[17] M. Notomi, E. Kuramochi, and T. Tanabe, Large-scale arrays of ultrahigh-Q coupled nanocavities, Nat. Photon. **2**, 741 (2008).

[18] Y. A. Vlasov, M. O'Boyle, H. F. Hamann, and S. J. McNab, Active control of slow light on a chip with photonic crystal waveguides, Nature (London) **438**, 65 (2005).

[19] H. Yoshimi, T. Yamaguchi, Y. Ota, Y. Arakawa, and S. Iwamoto, Slow light waveguides in topological valley photonic crystals, Opt. Lett. **45**, 2648 (2020).

[20] H. Yoshimi, T. Yamaguchi, R. Katsumi, Y. Ota, Y. Arakawa, and S. Iwamoto, Experimental demonstration of topological slow light waveguides in valley photonic crystals, Opt. Express **29**, 13441 (2021).

[21] L. Brillouin, *Wave Propagation and Group Velocity*, Pure and Applied Physics: a Series of Monographs, Vol. 8 (Academic Press, New York, 1960).

[22] L. J. Wang, A. Kuzmich, and A. Dogariu, Gain-assisted superluminal light propagation, Nature (London) **406**, 277 (2000).

[23] M. S. Bigelow, N. N. Lepeshkin, and R. W. Boyd, Superluminal and slow light propagation in a room-temperature solid, Science **301**, 200 (2003).

[24] R. W. Ziolkowski, Superluminal transmission of information through an electromagnetic metamaterial, Phys. Rev. E **63**, 046604 (2001).

[25] S. Xu, X. Cheng, S. Xi, R. Zhang, H. O. Moser, Z. Shen, Y. Xu, Z. Huang, X. Zhang, F. Yu, B. Zhang, and H. Chen, Experimental demonstration of a free-space cylindrical cloak without superluminal propagation, Phys. Rev. Lett. **109**, 223903 (2012).

[26] S. Longhi, Convective and absolute $\mathcal{PT}$-symmetry breaking in tight-binding lattices, Phys. Rev. A **88**, 052102 (2013).

[27] H. Schomerus and J. Wiersig, Non-Hermitian-transport effects in coupled-resonator optical waveguides, Phys. Rev. A **90**, 053819 (2014).

[28] K. Takata and M. Notomi, $\mathcal{PT}$-symmetric coupled-resonator waveguide based on buried heterostructure nanocavities, Phys. Rev. Appl. **7**, 054023 (2017).

[29] K. Takata, N. Roberts, A. Shinya, and M. Notomi, Imaginary couplings in non-Hermitian coupled-mode theory: Effects on exceptional points of optical resonators, Phys. Rev. A **105**, 013523 (2022).

[30] X. Cui, K. Ding, J.-W. Dong, and C. T. Chan, Exceptional points and their coalescence of $\mathcal{PT}$-symmetric interface states in photonic crystals, Phys. Rev. B **100**, 115412 (2019).

[31] A. Mock, Symmetry-engineered waveguide dispersion in $\mathcal{PT}$ symmetric photonic crystal waveguides, J. Opt. Soc. Am. B **37**, 168 (2020).

[32] Y.-T. Fang, S.-F. Ye, and X.-X. Li, Unique band coalescence and exceptional points from two-dimensional photonic crystal waveguide, J. Opt. **21**, 055103 (2019).

[33] Y. X. Zhao and A. P. Schnyder, Nonsymmorphic symmetry-required band crossings in topological semimetals, Phys. Rev. B **94**, 195109 (2016).

[34] H. C. Wu, L. Jin, and Z. Song, Topology of an anti-parity-time symmetric non-Hermitian Su-Schrieffer-Heeger model, Phys. Rev. B **103**, 235110 (2021).

[35] J. A. Iglesias Martínez, N. Laforge, M. Kadic, and V. Laude, Topological waves guided by a glide-reflection symmetric crystal interface, Phys. Rev. B **106**, 064304 (2022).

[36] Y. Plotnik, M. C. Rechtsman, D. Song, M. Heinrich, J. M. Zeuner, S. Nolte, Y. Lumer, N. Malkova, J. Xu, A. Szameit, Z. Chen, and M. Segev, Observation of unconventional edge states in 'photonic graphene', Nat. Mater. **13**, 57 (2014).

[37] T. Yoda and M. Notomi, Air-hole-type valley photonic crystal slab with simple triangular lattice for valley-contrasting physics, in *CLEO: Science and Innovations* (Optica Publishing Group, Massachusetts, 2019), p. JTh2A–10.

[38] I. Söllner, S. Mahmoodian, S. L. Hansen, L. Midolo, A. Javadi, G. Kiršanskė, T. Pregnolato, H. El-Ella, E. H. Lee, J. D. Song, S. Stobbe, and P. Lodahl, Deterministic photon–emitter coupling in chiral photonic circuits, Nat. Nanotechnol. **10**, 775 (2015).

[39] S. Mahmoodian, K. Prindal-Nielsen, I. Söllner, S. Stobbe, and P. Lodahl, Engineering chiral light–matter interaction in photonic crystal waveguides with slow light, Opt. Mater. Express **7**, 43 (2017).

[40] Z.-P. Liu, J. Zhang, S.K. Özdemir, B. Peng, H. Jing, X.-Y. Lü, C.-W. Li, L. Yang, F. Nori, and Y.-x. Liu, Metrology with $\mathcal{PT}$-symmetric cavities: Enhanced sensitivity near the $\mathcal{PT}$-phase transition, Phys. Rev. Lett. **117**, 110802 (2016).

[41] A. Cerjan, A. Raman, and S. Fan, Exceptional contours and band structure design in parity-time symmetric photonic crystals, Phys. Rev. Lett. **116**, 203902 (2016).

[42] A. H. Castro Neto, F. Guinea, N. M. R. Peres, K. S. Novoselov, and A. K. Geim, The electronic properties of graphene, Rev. Mod. Phys. **81**, 109 (2009).

[43] Y.-W. Tan, Y. Zhang, K. Bolotin, Y. Zhao, S. Adam, E. H. Hwang, S. Das Sarma, H. L. Stormer, and P. Kim, Measurement of scattering rate and minimum conductivity in graphene, Phys. Rev. Lett. **99**, 246803 (2007).

[44] W.-K. Tse, E. H. Hwang, and S. Das Sarma, Ballistic hot electron transport in graphene, Appl. Phys. Lett. **93**, 023128 (2008).

[45] M. Breusing, S. Kuehn, T. Winzer, E. Malić, F. Milde, N. Severin, J. P. Rabe, C. Ropers, A. Knorr, and T. Elsaesser, Ultrafast nonequilibrium carrier dynamics in a single graphene layer, Phys. Rev. B **83**, 153410 (2011).

[46] H. Wang, J. H. Strait, P. A. George, S. Shivaraman, V. B. Shields, M. Chandrashekhar, J. Hwang, F. Rana, M. G. Spencer, C. S. Ruiz-Vargas, and J. Park, Ultrafast relaxation dynamics of hot optical phonons in graphene, Appl. Phys. Lett. **96**, 081917 (2010).

[47] M. T. Mihnev, F. Kadi, C. J. Divin, T. Winzer, S. Lee, C.-H. Liu, Z. Zhong, C. Berger, W. A. de Heer, E. Malic, A. Knorr, and T. B. Norris, Microscopic origins of the terahertz carrier relaxation and cooling dynamics in graphene, Nat. Commun. **7**, 11617 (2016).

[48] G. W. Hanson, Dyadic Green's functions and guided surface waves for a surface conductivity model of graphene, J. Appl. Phys. **103**, 064302 (2008).

[49] A. Majumdar, J. Kim, J. Vuckovic, and F. Wang, Electrical control of silicon photonic crystal cavity by graphene, Nano Lett. **13**, 515 (2013).

[50] S. Satoshi, S. Otsuka, Y. Moritake, T. Yoda, T. Uemura, M. Ono, E. Kuramochi, and M. Notomi, Non-Hermitian chirality and topological properties of graphene-loaded photonic crystals, in *CLEO 2023* (Optica Publishing Group, 2023), p. FM4B.3.

[51] N. Parappurath, F. Alpeggiani, L. Kuipers, and E. Verhagen, Direct observation of topological edge states in silicon photonic crystals: Spin, dispersion, and chiral routing, Sci. Adv. **6**, eaaw4137 (2020).

[52] T. Uemura, Y. Moritake, T. Yoda, H. Chiba, Y. Tanaka, M. Ono, E. Kuramochi, and M. Notomi, Photonic topological phase transition induced by material phase transition, Sci. Adv. **10**, eadp7779 (2024).

[53] M. Barsukova, F. Grisé, Z. Zhang, S. Vaidya, J. Guglielmon, M. I. Weinstein, L. He, B. Zhen, R. McEntaffer, and M. C. Rechtsman, Direct observation of Landau levels in silicon photonic crystals, Nat. Photon. **18**, 580 (2024).

[54] M. I. Shalaev, W. Walasik, A. Tsukernik, Y. Xu, and N. M. Litchinitser, Robust topologically protected transport in photonic crystals at telecommunication wavelengths, Nat. Nanotechnol. **14**, 31 (2019).

[55] K. Sakoda and K. Sakoda, *Optical Properties of Photonic Crystals*, Vol. 2 (Springer, 2005).